Mon. Not. R. Astron. Soc. **000**, 000–000 (0000) Printed 7 May 2003 (MN LATEX style file v2.2)

Large scale galaxy distribution - observed and simulated

A.G. Doroshkevich[1,2], R.Fong[3], D.L. Tucker[4], & V.Turchaninov[2]
1 *Theoretical Astrophysics Center, Juliane Maries Vej 30, DK-2100 Copenhagen Ø, Denmark*
2 *Keldysh Institute of Applied Mathematics, Russian Academy of Sciences, 125047 Moscow, Russia*
3 *Dept. of Physics, University of Durham, Durham, DH1 3LE, England*
4 *Fermi National Accelerator Laboratory, MS 127, P.O. Box 500, Batavia, IL 60510, USA*

7 May 2003

ABSTRACT
The large scale galaxy distributions in the Las Campanas Redshift survey (LCRS) are investigated and compared with those in mock LCRS and mock 2dF catalogs and with simulated dark matter particles and 'galaxies' in a cubic volume. Results obtained with the Minimal Spanning Tree method reveal and statistically characterize the influence of (1) the galaxy identification procedure in numerical simulations, (2) the geometry of the survey volume, (3) the selection effects within a catalog, and (4) the random velocities of the large scale matter distribution. *** All these factors lead to the significant bias between the statistical characteristics of the basic DM and 'observed' galaxy distributions.

Some statistical characteristics of large scale DM and galaxy distributions and, in particular, its morphology are discussed and compared. We show that, in real space, the filamentary character of matter distribution dominates for all simulated catalogs and a moderate two-dimensional sheet-like component appears mainly within high density massive walls due to partial matter relaxation. However, even in real space, the quantitative characteristics of DM and 'galaxy' distributions are found to be quite different because of the sharp decrease of the number of objects. ***

In redshift space for the LCRS, mock LCRS, and mock 2dF catalogs, the sheet-like structures dominate and contain 70 – 90% of all galaxies. This means that the high density walls are formed by the successive compression and relaxation of earlier formed filaments and other structure elements, and even the moderate random re-positioning of galaxies due to radial velocities results stronly affects the *observed* internal characteristics of structure elements. The evidences in favor of such conclusion are seen in the observed galaxy distribution within the Great Wall (Fig. 5 in Ramella, Geller & Huchra 1992).

We show that low density models such as the flat ΛCDM model with the dimensionless matter density $\Omega_m \approx 0.3$, $\Omega_\Lambda \approx 0.7$, and the open CDM (OCDM) model with $\Omega_m \approx 0.5$ are well consistent, for the Hubble constant $h = H_0/100km/s/\mathrm{Mpc} \approx 0.65$, with the observed large scale galaxy distribution in the LCRS.

Key words: cosmology: large-scale structure of the Universe — galaxies: clusters: general – theory.

1 INTRODUCTION

Observationally, a striking picture has emerged for the form of large-scale structure, with galaxy redshift surveys revealing an intricate, random cosmic network of walls and filaments. It can be seen, for example, in the two surveys of concern here: the Durham/UKST Galaxy Redshift Survey (Ratcliffe et al. 1996, hereafter DURS) and the Las Campanas Redshift Survey (Shectman et al. 1996, hereafter LCRS). N-body simulations reinforce this picture, providing furthermore a web-like nature to the underlying dark matter (DM) distribution (see, e.g., Jenkins et al., 1998), but, importantly, also confirming that the large-scale structure we see in the Universe results from the growth through gravitational instability of small density inhomogeneities at the time of recombination (see, e.g., Cole et al. 1997, 1998). Our analyses show that, for the present epoch, walls are a major component of large-scale structure in the Universe, containing as many as ∼(40–50)% of the total galaxy population.

Most remarkable would be the Great Wall, a distinctly rich overdensity of galaxies seen in the CfA galaxy redshift survey and seeming to have a length of $\sim 100\,h^{-1}$ Mpc (de

Lapparent, Geller & Huchra 1988); it was originally termed a supercluster when observed by Thompson & Gregory (1978). But, walls are clearly interconnected and the Southern Sky Redshift Survey would even suggest that the Great Wall connects to the walls in the South Galactic Cap (da Costa et al. 1994; see, also, DURS). When viewed in projection on the sky, the Great Wall can itself be seen to be highly inhomogeneous, irregularly interwoven with rich filaments, with rich clusters or knots at intersections, and even with large 'holes' piercing the wall (see Fig. 5a of Ramella, Geller & Huchra 1992). Clearly, the size of walls is a rather arbitrary concept; quantitatively, we can only measure the size of the more overdense parts of walls. However, the walls are seen to surround generally large 'voids', $\sim 50\,h^{-1}$ Mpc in extent and containing poor galaxy filaments, creating a highly random and broken cellular structure, for which one might well hope to define a mean size for the 'cells' or voids.

Early discussions of the possibility of superclusters of galaxies being Zel'dovich pancakes, a general consequence of gravitational instability, were given by Thompson & Gregory (1978) and Oort (1983a, b). More recently, quantitative evidence for such a connection has come through a comparison of the statistical characteristics of simulated walls with the analytic predictions of an approximate model (Demiański & Doroshkevich 1999a, b, hereafter DD99; Demiański et al. 1999, hereafter DDMT). The model is based on the Zel'dovich Approximation (Zel'dovich 1970, 1978; Shandarin & Zel'dovich 1989), which has been shown in N-body simulations to trace faithfully the growth of structure under gravitational instability well into the non-linear regime, failing only on small scales in regions in which the particles have begun the process of virialization. The model predicts that structure evolution can be roughly described as a hierarchical formation of Zel'dovich pancakes. Indeed, a pancake describes generally how structure begins to form, as one axis begins to collapse more rapidly than the other two. But, for the first structures, collapse soon also occurs along a second axis to produce filaments. These filaments are also collapsing towards each other into larger and richer pancakes. These large rich pancakes are then Zel'dovich pancakes still in their first evolutionary stage and are, thus, now seen as systems interwoven with high density filaments and clumps, as we saw above for the Great Wall.

There are now several methods for the quantitative analysis and description of such a complex galaxy distribution. The methods explore different properties of the distribution, thus complementing each other. The most broadly used and most studied analysis is that of the two-point correlation function (Peebles 1993) and its Fourier transform, the power spectrum. It is the most basic analysis for studying the clustering of any point distribution. At present, it reliably characterizes the galaxy distribution on scales of $\lesssim 10\,h^{-1}$ Mpc, but a large effort is ongoing to extend its possibilities to much larger scales through power spectrum analysis. Some information about the galaxy distribution on such larger scales has been obtained with percolation analysis (Zel'dovich, Einasto & Shandarin 1982), the genus curve (Gott, Melott & Dickinson 1986), core sampling analysis (Buryak, Doroshkevich & Fong, 1994, Doroshkevich et al. 1996, hereafter Paper 1) and with Minkowski functionals (Sahni, Sathyaprakash, & Shandarin 1998; Sathyaprakash, Sahni & Shandarin 1996, 1998; Schmalzing et al. 1999; Schmalzing & Diaferio 1999; Bharadwaj et al. 2000).

However, considering that the cosmic web we see is primarily made up of sheet-like and filamentary structures, perhaps the most promising analysis for a quantitative description of such structures is that of the graph theoretical technique of the Minimal Spanning Tree (Barrow, Bhavsar, & Sonoda 1985; van de Weygaert 1991). Its effectiveness for the analysis of observations is already clear from the work of Bhavsar & Ling (1988), who successfully applied it to extract filamentary structures from the original CfA Redshift Survey (de Lapparent, Geller, Huchra 1988). More recently, we have successfully applied Minimal Spanning Tree analysis to simulated DM distributions (Doroshkevich et al. 1999, hereafter DMRT) and to observational redshift catalogs, the LCRS (Doroshkevich et al. 2001, hereafter Paper 2) and the DURS (Doroshkevich et al. 2000). The MST approach includes also several methods allowing the measurement of complementary characteristics of structure. These methods are presented in Sec. 2.

In this paper we take our study of the MST approach a stage further and apply it to mock 'galaxy' catalogs based on N-body simulations (Cole et al. 1998), as well as to the LCRS observed catalogue. The mock catalogs not only identify 'galaxies' through standard biasing algorithms, but the 'galaxies' have been assigned absolute magnitudes based on an observed galaxy luminosity function, and thus the catalogs have a realistic observational galaxy selection function appropriate for magnitude limited samples. Of course, both the mock and observed catalogs have already been studied with various other methods, including correlation function and power spectrum analyses (see, e.g., Landy et al. 1996; Ratcliffe et al. 1996, 1998; Tucker et al. 1997; Paper 1; Shandarin & Yess 1998; Cole et al. 1998; Paper 2; Doroshkevich et al. 2000).

In their application of the MST analysis to DM catalogs from N-body simulations, DMRT established that, indeed, the measures obtained do correspond approximately to theoretical parameters of large-scale structure that can be derived using the Zel'dovich Approximation (DD99). They also showed that, for models like SCDM, structure is much too evolved compared to that seen today. For this paper, we have thus concentrated on the currently favoured models of Lambda CDM (ΛCDM) and Open CDM (OCDM).

However, because of biasing, the distribution of galaxies will differ from that of DM. We have thus also analysed the underlying N-body simulations of the mock catalogs (kindly supplied by S. Cole) to determine the possible effect biasing has on our measures. Furthermore, with the simulations, we can also determine the difference in the results from analyses of the distributions in real as well as in redshift space. Finally, the analysis of the mock catalogs will allow us to determine the effect of the selection functions for our observational catalogs. The results of this analysis are also compared to the results for the actual observational survey, the LCRS.

This paper is organized as follows: In Sec. 2 the methods used are introduced. Sec. 3 briefly describes the basic simulated and observed catalogs. General characteristics of the MSTs for these catalogs are given in Sec. 4 and the properties of selected structure elements discussed in Sec. 5. We present in Secs. 6 &,7 a more detailed comparison of

the observed and simulated structure elements. Finally, we conclude with a summary and short discussion of the main results in Sec. 6.

2 CHARACTERISTICS OF LARGE SCALE MATTER DISTRIBUTION

In this section we describe the techniques that we shall be using. The Minimal Spanning Tree (MST) is powerful technique which allows us to obtain detailed characteristics of sample of objects. It is also closely related to the more familiar friends-of-friends clustering analysis; given the MST for the whole sample, the cluster sample for a particular linking length, l, is obtained by simply *separating* the MST with respect to l – i.e., by removing any edges from the MST whose length exceeds l gives the 'friends-of-friends' cluster catalog for that linking length. Basically, the MST for a galaxy distribution contains within it all 'friends-of-friends' cluster catalogs for all linking lengths. It also makes the MST analysis a powerful method for a more intensive usage of clustering analysis. In our case, it helps separate the high density regions from the low, with the high density regions expected to be wall dominated and the low density regions expected to be filament dominated. We can then test these expectations by applying the MST technique to each density regime, as well as to individual clusters.

As the techniques described apply to all samples, we shall here simply refer to the objects in a sample as 'points'. Thus, depending on the sample, they are either DM particles, simulation 'galaxies', or observed galaxies.

2.1 Minimal Spanning Tree technique and cluster analysis

The MST construct is a graph theoretical technique, originally introduced by Kruskal (1956) and Prim (1957) and widely applied in telecommunications and similar fields. For a given point sample, it is a *unique network* connecting all the points of a sample such that the total length of the network is a minimum, resulting generally in a tree-like structure. Some definitions, examples, and applications of the technique can be found in Barrow, Bhavsar, & Sonoda (1985) and van de Weygaert (1991), with the latter also providing references to more detailed mathematical results. Here, we are mainly concerned with the *probability distribution function of the MST edge lengths*, W_{MST} (which we hereafter call the PDF MST method). Clearly then, the potential of the MST approach is not exhausted by our applications here.

The PDF MST, W_{MST}, depends, of course, on the correlation functions (or cumulants) of all orders. Most interestingly, for *large enough separations*, when correlation functions become small and the cumulants tend to constants, the distribution is expected to resemble a Poisson-like point distribution (White 1979; Buryak et al. 1991; Borgani 1996). Now, for one-dimensional filaments and two-dimensional sheets on which points are Poisson distributed, the PDF MSTs have particularly simple analytical forms (Kendall & Moran 1963); these are, respectively,

$$W_{MST}(x) = e^{-x}, \quad x = l_{MST}/\langle l_{MST}\rangle, \tag{2.1a}$$

$$W_{MST}(x) = 2xe^{-x^2}, \quad x^2 = l^2_{MST}/\langle l^2_{MST}\rangle), \tag{2.1b}$$

where l_{MST} is an edge length of the MST.

As we only expect this to hold on large scales, $\langle l_{MST}\rangle$ will be distorted by clustering on smaller scales, so we need then to fit our measured PDF MST with slightly modified exponential and Rayleigh distributions:

$$W_{MST} = e_1 \exp(-e_2 x), \; W_{MST} = c_1 x \exp(-c_2 x^2), \tag{2.2}$$

where e_2 and c_2 take this distortion into account and e_1 and c_1 are normalization factors. Thus, if, as noted in Paper 2 and DMRT, the PDF MST on the large scales of the observed and simulated point distributions is similar to a superposition of these functions, it would then provide quantitative corroboration for filaments and sheets as morphological characterizations of large-scale structure elements.

It is worth remarking that the technique then allows us to characterize the structure of a *whole* sample or of a subsample without the need of first separating out 'structure elements'. In Sec. 2.3 below we introduce a characteristic parameter of the MST useful for understanding the possible morphology of individual structure elements.

2.2 Selection of structure elements

Our previous analyses have shown that ∼(40–50)% of the total galaxy population are to be found in walls. We need then to apply a clustering analysis to divide the sample into two subsamples: a high density region dominated by walls, and a low density region composed of so-called 'voids', which we expect are dominated by poorer galaxy filaments. It will also be interesting to study the morphologies of the separate structure elements, i.e. the clusters themselves (Sec. 2.3).

As we mentioned at the beginning of Sec. 2, the complete set of clusters for a given linking length, l, is obtained by simply *separating* the MST with respect to l. For our purposes we use the two parameter method described and exploited in Doroshkevich et al. (2000) and Paper 2 for the observations and in DMRT for DM catalogs from N-body simulations. In this method the structure elements are identified with clusters found for a given threshold linking length, l_{th}, and a given threshold richness, N_{th}. The threshold linking length characterizes the threshold overdensity, δ_{th}, of the boundary of the cluster by

$$\delta_{th} = b_{th}^{-3} = \frac{3}{4\pi\langle n_{gal}\rangle l_{th}^3}, \tag{2.3}$$

where $\langle n_{gal}\rangle$ is the mean density of points in the sample and b_{th} is a dimensionless linking length. The threshold richness, N_{th}, allows us to select a set of clusters with a given range of richnesses. [Note that "friends-of-friends" group algorithms use a very similar terminology: e.g., Ramella, Geller, & Huchra (1989), for their group catalog, chose a linking length of $0.27\,h^{-1}$ Mpc equivalent to a threshold density $\delta_{th} \approx 80$, and a threshold richness of $N_{th} = 3$.]

As found in our previous papers a threshold overdensity $\delta_{th} = b_{th} \approx 1$ is convenient for the investigation of large scale structure. Physically, this is entirely reasonable for DM, as this divides underdense regions (relative to the mean density) from the overdense regions. Such underdense regions will expand more rapidly than the universe as a whole to form the voids we see today, whilst the overdense regions

will expand less rapidly, so collapse in comoving space, and will contain the rich wall-like structures of today. For observational catalogs, some variations in the values for b_{th} permit us to take into account a possible large scale bias (either natural or artificial) between the spatial distribution of galaxies and the dominant DM component.

The wall-like structure elements are usually identified with richer clusters. For a given b_{th} (or, equivalently, a given δ_{th}), choosing a threshold richness, N_{th}, such that the fraction of points $f_p \sim 0.4$–0.5, will provide a set of clusters that are associated with walls. The remaining galaxies in the catalog constitute the subsample of poorer structure elements. The MST study of these high density and low density subsamples then provides an insight into the separate morphological characteristics of the set of richer structure elements and the set of poorer ones.

2.3 Morphology of structure elements

Once a set of structure elements have been thus selected, each can be characterized, for example, by its richness or mass (in which each galaxy or DM particle is weighted equally), the sizes along the three principal axes of its inertia ellipsoid and its shape or morphology. Here we are simply interested in the morphology of a cluster.

The use of Minkowski functionals for determining morphological characteristics of large-scale structure elements has been discussed by Sahni, Sathyaprakash, & Shandarin (1998); Sathyaprakash, Sahni & Shandarin (1996, 1998); Schmalzing et al. (1999); Schmalzing & Diaferio (1999); and Bharadwaj et al. (2000). These methods can clearly characterize the shape of isodensity surface of structure elements.

Our interest in this paper, however, is to explore the usefulness of the MST technique. We will use for a cluster the appealing parameter, L_{tr}/L_{sum}, where L_{tr} is simply the full length of the *trunk* of the MST (i.e., the maximum continuous path in the tree) and where L_{sum} is the total sum of all the edges within the tree (*branches* included). This ratio characterizes then the shape of even curved structure elements and is applicable to both rich and poor clusters. As was discussed in Paper 2, we would expect $L_{tr}/L_{sum} \ll 1$ for sheet-like structure elements and elliptical clouds and $L_{tr}/L_{sum} \approx 1$ for filaments. Thus, the mass distribution as a function of this ratio, $F_m(L_{tr}/L_{sum})$, provides a suitable morphological description of the cluster catalog. In contrast to Minkowski functionals, this approach takes proper account of the point distribution within cluster rather than only the shape of isodensity surface.

Unfortunately, our results will show that we do not have such a clean separation of morphologies. Visually, we seem able to divide the elements of large-scale structure into sheets and filaments. However, in reality, the morphology of structure is much more complex. Even visually, we have seen how the most famous sheet-like structure, the Great Wall, seems to be composed of rich clusters bridged together by galaxy filaments, and it would seem that many clusters are composed of both filamentary and sheet-like components randomly combined. In reality then there is a continuous distribution of morphology, and it would be more accurate to discuss the *degree of filamentarity* and the *degree of a "wall-ness"* for a set of clusters. In this sense, the function $F_m(L_{tr}/L_{sum})$ provides the optimal characteristic of a sample under consideration.

2.4 Selection function

As both the observed and simulated mock catalogs are apparent magnitude limited, the apparent density of galaxies decreases with the distance according to the galaxy selection function. Normally, in friends-of-friends analyses some correction can be made by using a linking length that is distance dependent. More convenient for our MST analysis is the use of the following equivalent method.

For the simple magnitude-limited catalogs considered here the differential number count can be well fitted to the expression (Baugh & Efstathiou 1993)

$$dN_{gal}(x) = n(x)\,dx \propto x^2 \exp(-x^{1.5})dx,\ x = r/R_{sel}, \quad (2.4)$$

where r is the galaxy radial coordinate and the typical scale R_{sel} depends on the magnitude limit of the catalog. We can then create a *modified* galaxy catalog that is homogeneous by using the modified radial coordinate, $r_a(r)$, instead of the real radial coordinate, r:

$$r_a^3 = \int_0^r f_s dr = 2R_{sel}^3(1-(1+y)e^{-y}), \qquad (2.5)$$

$$y = \left(\frac{r}{R_{sel}}\right)^{1.5}.$$

For $r \ll R_{sel}$, $y \ll 1$, and $r_a \approx r$.

The procedure significantly improves the estimates for structure parameters such as the mass function of structure elements. However, it clearly cannot correct for the paucity of galaxies in the most distant part of a survey, where it would produce a significant fraction of spurious clusters. In practice the volume of a redshift survey in which cluster analysis can sensibly be used is restricted by both a small distance cutoff, D_{min}, below which significant numbers of clusters are seriously truncated by the survey boundaries, as well as a large distance cutoff, D_{max}. (Again, this is similar to the situation with standard "friends-of-friends" groups algorithms: even though one can scale the linking lengths to take into account selection effects in redshift surveys, beyond a certain redshift the resulting groups are increasingly likely to be spurious.)

For some catalogs (e.g., the LCRS), a bright apparent magnitude cutoff was also used. In this case, the four parameter relation for the selection function can be written as a difference between two functions similar to (2.4), but with different R_{sel} and different normalization. However, taking into consideration the approximate character of this process of 'correcting' for the galaxy selection function – as well as the need to impose these minimal and maximal depths – we will fit the observed galaxy distribution for such catalogs with a three parameter function that is the same as equation (2.4) except for the substitution of $x - x_0$ in place of x, with $x_0 \le D_{min}/R_{sel}$.

2.5 Spatial distribution of structure elements

Perhaps the most widely known early example of characterizing the spatial distribution of wall-like structures within

the free path of a narrow pencil beam redshift survey is that of Broadhurst et al. (1990). *** It was thus that Buryak et al. (1994) proposed another implementation of the quantitative analogue to the visual identification of clusters in deep narrow pencil beam redshift surveys – that of the core-sampling technique. The details of this technique can be found in Paper 1, where it was applied to the deep wedge slices of the LCRS. The core-sampling method was thus also applied to the DURS (Doroshkevich er al. 2000). ***

A simple form of the core-sampling method was used in DDMT to characterize properties of the wall-like structures for simulated dark matter catalogs and mock galaxy catalogs. The application of this simple form of the core-sampling method assumes that all galaxies in the sample are distributed either in a set of conic cores with a given angular size θ_{core} or in a set of cylinders with a given diameter D_{core}. All galaxies are projected onto the core axis and the one-dimensional distribution of galaxies along this axis is investigated. In each core, the galaxies are grouped – with appropriate linking lengths – into point-like clusters placed at their centres-of-mass. The estimate of the mean free path is then just the average separation between these cluster points along the cores.

Two factors restrict the application of this method for deep surveys. Firstly, the linear diameter of a conic core increases quickly with distance and, for distant regions, multiple structures will overlap in projection onto the core axis. This overlapping distorts the measured separation and, in fact, destroys the main idea behind the core-sampling approach. At the other extreme, the small linear size of conic core at small distances does not provide the effective averaging of structure characteristics over the core. For such cores the small scale clustering of galaxies within walls distorts results and increases its random scatter.

To suppress the action of these factors and to obtain more robust estimates of the free path we can, for example, investigate nearby and distant regions separately.

2.5.1 Mean free-path between wall-like elements

Following the main ideas of the core-sampling approach, we will find the set of the separations for walls along random cores (the free path) both in the radial and in the transverse directions. The main advantage of such an approach is to look at the same sample at two complementary orientations. The arbitrary character of such a definition of separation is an inevitable consequence of the irregular shape and distribution of richer clusters.

2.5.2 Characteristics of random network of filaments

The characteristics of the spatial distribution of filaments are more complicated as filaments form a random broken network. The mean free path between filaments depends upon the core shape as the number of filaments crossing the core increases proportionally to the core surface area. One useful property is the surface density of filaments, σ_f, which is the mean number of filaments intersecting a unit area of arbitrary orientation. This definition is insensitive to the linking of the filaments to joint network and thus yields an objective characteristic of this network.

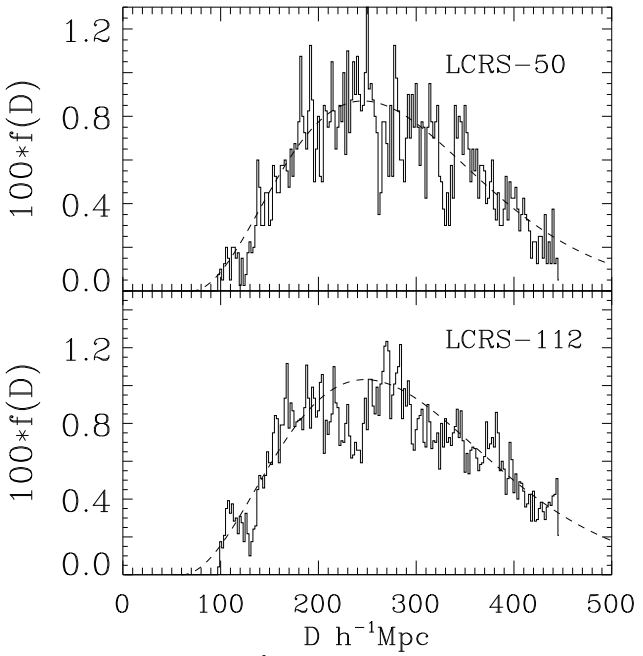

Figure 1. Distribution of galaxy distances in the two LCRS subsamples (50 and 112 fiber). The fits (2.4) and (3.1) are plotted by dashed lines.

As was found in Buryak et al. (1994) the surface density of filaments and the measured mean free path, $\langle D_{sep}\rangle$, are linked by expression

$$\sigma_f^{-1} = 0.5(S/L_{core})\langle D_{sep}\rangle, \qquad (2.6)$$

where S is the surface area and L_{core} is the length of the core. For conic and for cylindrical cores, respectively, this expression can be rewritten as follows:

$$\sigma_f^{-1} = 0.25\pi\theta_{core}(D_{min} + D_{max})\langle D_{sep}\rangle, \qquad (2.7a)$$

$$\sigma_f^{-1} = 0.5\pi D_{core}\langle D_{sep}\rangle, \qquad (2.7b)$$

where D_{min} and D_{max} are minimal and maximal depths of the core and θ_{core} and D_{core} are angular and linear diameter for conic and cylindrical cores, respectively.

3 BASIC OBSERVED AND SIMULATED CATALOGS

In this paper we investigate and compare the structure characteristics obtained for the observed catalog– the LCRS – *** *** sets of mock catalogs (Cole et al. 1998) simulating the 2dF survey. For the LCRS and DURS the general properties of the spatial galaxy distribution have been discussed in Paper 2 and in Doroshkevich et al. (2000).

3.1 Las Campanas Redshift Survey

The LCRS is organized as a set of 6 slices, three of which – the LCRS-1 ($\delta = -3°$), LCRS-2 ($\delta = -6°$), and LCRS-3 ($\delta = -12°$) – are located towards the Northern Galactic Cap, and other three slices – the LCRS-4 ($\delta = -39°$), LCRS-5 ($\delta = -42°$), and LCRS-6 ($\delta = -45°$) – are located towards the Southern Galactic Cap. Each slice consists of a

Table 1. Characteristics of observed and simulated catalogues

	Ω_m	h	N_{gal}	σ_8	$\sigma_{vel}/\sqrt{3}$ km/s	$\langle l^{real}_{MST}\rangle$ h^{-1}Mpc	$\langle l^{red}_{MST}\rangle$ h^{-1}Mpc
L3 Cubic Volume Catalogs							
DM	0.3	0.65	$7.08\cdot10^6$		471	0.65	
gal	0.3	0.65	$2.10\cdot10^6$		471	0.85	
Mock 2dF Catalogs							
O5-600	0.5	0.6	$1.85\cdot10^5$	0.9	471	1.68	1.91
L2-600	0.2	0.75	$1.60\cdot10^5$	0.9	336	2.20	2.26
L3-600	0.3	0.65	$1.59\cdot10^5$	1.05	451	2.02	2.14
L3-400	0.3	0.65	$0.99\cdot10^5$	1.05	418	1.56	1.67
Mock LCRS Catalogs							
lcrs-1	0.3	0.65	4656	1.05	382	2.42	2.53
lcrs-2	0.3	0.65	5126	1.05	406	2.39	2.50
lcrs-3	0.3	0.65	4388	1.05	377	2.55	2.62
lcrs-4	0.3	0.65	3541	1.05	371	2.55	2.69
LCRS			21352				2.70

Here $\langle l^{real}_{MST}\rangle$ and $\langle l^{red}_{MST}\rangle$ are the mean edge lengths of the full samples in real space and redshift space, respectively.

set of fields of angular size $1.5^\circ \times 1.5^\circ$. A detailed description of the LCRS can be found in Shectman et al. (1996). Some characteristics of large scale galaxy distribution were discussed in Paper 1 and Paper 2.

One part of the survey ($\approx$ 80% of the galaxies) was performed with 112 fibers in each field and includes galaxies within a nominal apparent magnitude range of $15.0 < m_R \leq 17.7$, but the other part ($\approx$ 20% of galaxies) was performed with 50 fibers in each field and includes galaxies within a nominal range of $16.0 < m_R \leq 17.3$. Thus, the number of galaxies in a 112-fiber field is roughly twice that in a 50-fiber field. This factor causes artificial nonhomogeneities in the observed galaxy distribution. For other slices the richer and poorer fields are intermixed, and this partially disrupts the regular character of observed structures and decreases the mean observed density of galaxies by about 20%.

Another peculiarity of the LCRS is a depression of the number of close galaxy pairs due to the finite size of fibers (55 arcsec on the sky). This 'fiber separation effect' partly eliminates the small scale clustering of galaxies and artificially reduces the measured richness of highly density clumps. The random selection of galaxies within richer fields up to 112 or 50 objects, respectively, decreases also the richness of walls.

Of course, these artificial selection effects could distort the measured characteristics of walls in the LCRS. But as discussed below, the influence of small angular thickness of slices and limited representativity of the LCRS seems to be more important and can result in stronger random variations of measured structure characteristics. This means that results obtained for this catalog have a *preliminary* character, and such analysis must be repeated for more representative (and homogeneous) surveys.

For this catalog the selection function (2.4) can be used with a redefined dimensionless distance as follows:

$$x = r/R_{sel} - 0.44, \quad R_{sel} = 150h^{-1}\mathrm{Mpc}. \qquad (3.1)$$

A modified catalog with the galactic density independent of distance can be constructed as described in Sec. 2.5 . The best sampled part of the LCRS are situated at distance $D \approx 250h^{-1}$Mpc (Fig. 1).

*** ***

3.2 Basic simulations

Here we consider four COBE-normalized magnitude-limited mock catalogs (Cole et al. 1998) simulating the 2dF survey. Catalogs L2 & L3 are based on the flat ΛCDM model whereas the catalog O5 is based on the OCDM model. We restrict the catalogs L2-600, L3-600, & O5-600 to depths of $100h^{-1}\mathrm{Mpc} \leq D \leq 600h^{-1}$Mpc and the catalog L3-400 to depths of $100h^{-1}\mathrm{Mpc} \leq D \leq 400h^{-1}$Mpc (i.e., ∼62% of galaxies and ∼30% of volume of the sample L3-600). All these catalogs are investigated both in real space and in redshift space. These catalogs permit us to test our methods for various cosmological models with realistic selection and geometrical effects characteric of observational catalogs.

The basic DM distribution and its corresponding sample of simulation 'galaxies' in a cubic volume are used for the comparison with these mock catalogs. Such comparison allows us to investigate the influence of the process of galaxy identification within N-body simulations and the influence of the usual observational selection effects on the measured properties of the large scale matter distribution.

All mock catalogs reproduce the main observed characteristics of large scale matter distribution. They have been prepared with the same set of random amplitudes and differ only by the evolutionary degree attained. In all models the general large scale structure is similar, differing only by the degree of galaxy condensation and by the density contrast. For all catalogs the selection effects are well described by Eq. (2.4) with the typical scale $R_{sel} = 288h^{-1}$Mpc. The best sampled regions are located near $300h^{-1}$Mpc.

The main characteristics of these catalogs are listed in Table 1, where N_{gal} is the number of 'galaxies', σ_8 is the amplitude of perturbations used, and σ_{vel} is the velocity dispersion of all the 'galaxies'.

For comparison with the LCRS, four slices with angu-

lar size $\delta = 1.5°$ and magnitudes $16.15 \leq m \leq 18.5$ were extracted from the ΛCDM simulation with Ω_m=0.3 for a maximum depth of $400h^{-1}$Mpc. For these slices the number of galaxies and the selection function are similar to those in the LCRS. Parameters of these slices are also listed in Table 1. *** We find most of the results for the models to be similar and so will discuss just the results from the ΛCDM with $\Omega_m = 0.3$ simulation. ***

4 GENERAL PROPERTIES OF LARGE-SCALE STRUCTURE

In this section we study the MSTs for the simulations, applying the MST analysis to each catalog as a whole. *** ***

With the mock catalogs, we are also able to make comparisons of some of the properties in the simulations with the corresponding results for the two observational catalogs, the LCRS (Paper 2) and DURS (Doroshkevich et al. 2000).

However, the main aim of our study here is to explore the effect on our MST analysis due to (a) the 'biasing' applied in these simulations to identify 'galaxies', (b) the difference between real and redshift space, and (c) the observational constraints in magnitude limited redshift surveys due to both the galaxy selection function and a wedge-shaped spatial geometry.

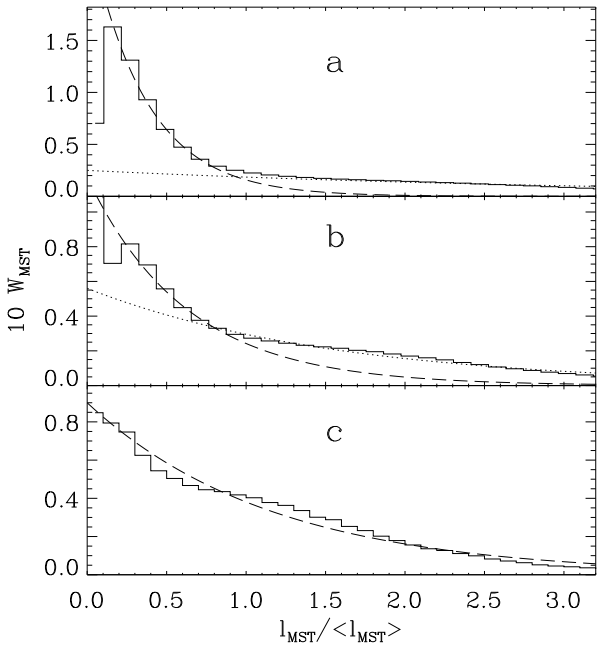

Figure 2. Distribution functions of MST edge lengths in real space for the basic distribution of DM particles (panel a), volume-limited distribution of galaxies in a cube (panel b), and for the $L3-600$ mock 2dF catalog (panel c), Two exponential fits are plotted by dashed and dotted lines.

4.1 Minimal Spanning Tree in real and redshift spaces

4.1.1 DM and 'galaxy' distributions in real space

Figures 2a & b show the MST PDFs for the DM and 'galaxy' distributions in the full cube of the ΛCDM simulation. In both cases, the MST PDFs are well fitted by two exponentials, one for $l^{real}_{MST} \lesssim \langle l^{real}_{MST}\rangle$ and the other for $l^{real}_{MST} \gtrsim \langle l^{real}_{MST}\rangle$, *** with a some moderate fraction of high density clumps with $l^{real}_{MST} \lesssim 0.1\langle l^{real}_{MST}\rangle$. *** Here $\langle l^{real}_{MST}\rangle$ is the mean edge length for the whole population, the values of which are listed in Table 1. (Note: in Table 1, l^{real}_{MST} denotes the *real space* linking length; l^{red}_{MST} denotes *redshift space* linking length.) Thus, the MST analysis describes both the DM and 'galaxy' spatial distributions as two different systems of filamentary structure elements. (Recall from eq. 2.1a that an exponential fit indicates a one-dimensional, or filamentary, distribution.)

Fig. 2a furthermore shows that most of the DM (∼90% of the DM particles) is in the denser filaments. The exponential fits give mean edge lengths of $\sim 0.4\langle l^{real}_{MST}\rangle$ for this subpopulation and $\sim 3\langle l^{real}_{MST}\rangle$ for the lower density filaments. Fig. 2b, on the other hand, shows that the numbers of 'galaxies' in the high and low density populations are more comparable, with ∼75% 'galaxies' in the denser filaments. The fits give mean edge lengths of $\sim 0.6\langle l^{real}_{MST}\rangle$ for this subpopulation and $\sim 2\langle l^{real}_{MST}\rangle$ for the other 'galaxies'. This difference between the DM and 'galaxy' distributions is, of course, a direct consequence of the 'anti-biasing' procedure used by Cole et al. (1998) for identifying which DM particles are 'galaxies'. It effectively suppresses the cluster cores that CDM forms, which have been found to have a much steeper central profile than observed for the cores of galaxy clusters.

The effect of imposing on the 'galaxy' distribution the selection function and the spatial wedge geometry of an observed magnitude limited sample can be seen in Fig. 2c, where the MST PDF for the mock 2dF 'galaxy' catalog L3-600 is plotted. It shows a much smoother distribution of edge lengths which can be approximately fitted to a single exponential function with the same $\langle l^{real}_{MST}\rangle$ as for the population in the corresponding observational catalogs (Table 1). The small excess of edges over the exponential fit, with $l/\langle l^{real}_{MST}\rangle \approx$1–2, would seem to indicate the existence of a relatively weak wall-like component. But, clearly, the imposition of the observational constraints has caused a major distortion of the MST PDF. Attempting to account for the selection effect through the use of the 'modified' catalog (see Sec. 2.4) does help to decrease the mean edge length by about 1.5 times, but it remains 1.5 times larger than the $\langle l^{real}_{MST}\rangle$ for the volume-limited 'galaxy' distribution in the simulation cube. In any case, *** *** it has been unable to correct the general shape of the MST PDF fully.

In summary, the results of this section show how the MST analysis sensitively reflects the biasing between 'galaxies' and DM. However, they also show how the constraints of real observations greatly alter the large-scale characteristics of the galaxy distribution. Statistical measures, such as the correlation function or power spectrum analysis, can be corrected for the selection function and the observational 'window'. However, such measures are averages over the sample, which the MST is not. Thus, the MST, as we have seen, cannot be effectively corrected by the procedure that is often used for constructing cluster catalogs; it simply reflects the rather obvious fact that one cannot truly restore lost

information and thereby fully reconstruct the full and true galaxy distribution in the universe.

4.1.2 Galaxy distributions in redshift space

Here, we describe the MST PDFs in redshift space for four catalogs, including that for the observed LCRS, which is plotted in Fig. 3a. This can then be directly compared with the mock LCRS, a catalog of four slices from the ΛCDM simulation, the results of which are plotted in Fig. 3b. There is little difference in the results whether we use the mock 2dF limited to $400\,h^{-1}$ Mpc or $600\,h^{-1}$ Mpc. Also, similar to the results in the previous section on the real space distributions, using the 'modified' catalogs based on these redshift space ones decreases the mean edge length by a factor of about 1.7–2 times, but changes little the form of the MST PDFs.

In contrast to real space, most of the MST PDF of the redshift space distribution for each catalog is well fitted by a Rayleigh function (eq. 2.1b), indicating the domination of a sheet-like component for denser clusters. Only for larger $l_{MST} \geq 1.5\ \langle l_{MST}\rangle$ does an exponential distribution of edge lengths appear, consistent with the presence in redshift space of low density filaments containing only 10–30% of the galaxies. Of course, in the transitional region, near $l_{MST} \approx 1.5\ \langle l_{MST}\rangle$, any discrimination between sheet-like and filamentary components would be rather arbitrary. We can see from the Rayleigh function fits at smaller values of l_{MST} that ∼70 – 90% of galaxies are concentrated within wall-like *** and elliptical *** clusters and the remaining ∼10 – 30% of galaxies relate to the filamentary component. The fraction of galaxies assigned to wall-like clusters is least for the LCRS (∼67%), gradually increases for the mock LCRS (∼80%), and reaches ∼90% for the L3-400 and L3-600 samples.

However, the interesting consideration is in the change caused by the transition from real space to redshift space, which can be seen directly in Figs. 2c and 3c for the mock 2dF samples, L3–600. In Fig. 2c, we see only filaments, whereas Fig. 3c contains a substantial fraction of the sheet-like structures. The simplest explanation is that these walls we see in redshift space are actually made up of high density filaments, which are so close that the small displacements of the galaxies caused by their random peculiar velocities, ∼ 300 km s^{-1}, have 'merged' or 'smeared' the filaments together into sheet-like structures, with such velocities corresponding to displacements $\sim 3\,h^{-1}$ Mpc$\approx 2\langle l_{MST}\rangle$. Thus, we expect that the great walls of galaxies observed in galaxy redshift surveys to be highly inhomogeneous, and indeed this is exactly what we see for the 'Great Wall' in the North Galactic Cap (Fig. 5a of Ramella, Geller & Huchra, 1992). Of course, this is also the reason why the autocorrelation function in real space is steeper than it is in redshift space (Davis & Peebles 1983, Baugh 1996).

Fig. 3b shows the MST PDF for the mock LCRS catalog of four slices extracted from the simulated mock 2dF catalog using the observational constraints of the actual LCRS. Comparing with Fig. 3a, it can be seen that the PDFs for this and the LCRS are similar. In both cases, the main fraction of galaxies are well fitted by Rayleigh functions, with a relatively small fraction, ∼20–30%, in the one-dimensional filamentary – i.e., exponential – 'tails' of the PDFs. ***

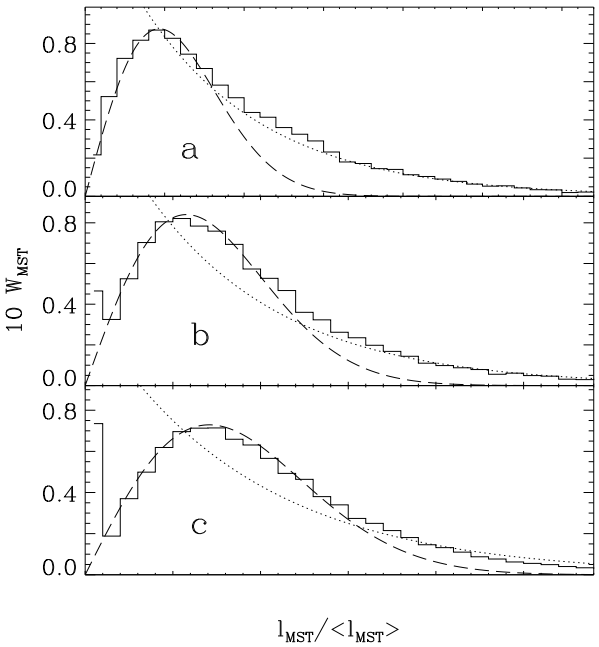

Figure 3. Distribution functions of MST edge lengths in redshift space with correction for the selection effect for the average of the six slices of the observed LCRS catalog (panel a), for the average of the four slices of the ΛCDM mock LCRS catalog (panel b), and for the ΛCDM-600 mock 2dF catalog (panel c). Rayleigh fits are plotted by long dashed lines, exponential fits are plotted by dotted lines.

4.2 Mass functions of structure elements

***

The most basic characteristic of structure elements is their mass function. Here we are concerned with the richer structure elements most of which are far from a dynamical state of stable equilibrium. For such elements both Press-Schechter theory and Zel'dovich approximation (Demiański & Doroshkevich 2002) predict the same behaviour of the mass function,

$$W_m(\mu) \propto \exp(-\mu^{1/3}), \quad \mu = M/\langle M\rangle\,,$$

which can be tested with the available dataset.

These measured properties of separate elements of large-scale structure, i.e., clusters, will, of course, depend on the linking length used to define the clusters. They are, thus, not as well defined as the above characteristics for the DM and galaxy distributions as a whole. Nevertheless, using some predetermined fixed dimensionless linking length, b, and correcting for the effect of the galaxy selection function, the resulting measures seem to be sufficiently representative. Clearly, all clusters have $b > 1$, making $b = 1$ a natural choice for such a study of the global aspect of large-scale structure. Thus, we compare in this section these characteristics of separate structure elements selected in the observed LCRS and in the mock LCRS samples that we have constructed out of four slices of the L3-400 simulation catalog. To examine the effect caused by the use of slices rather than the wedge geometry of a large area of sky survey, we also compare the latter results with those for the mock 2dF samples, L3-400 . The analyses have, of course, all been applied to the 'modified' forms of the catalogs, in order to take into account the effect of the selection function (Sec. 2.4).

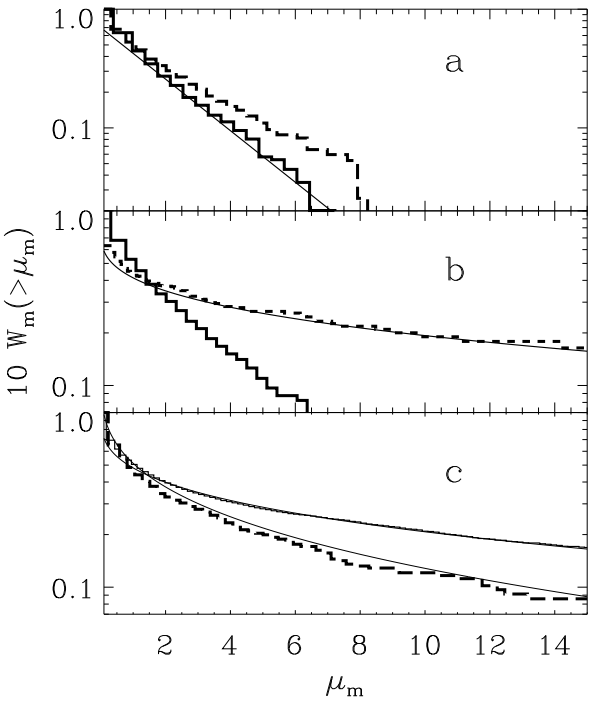

Figure 4. Cumulative mass functions of structure elements, $W_m(\geq \mu_m)$, at b_{thr}=1 for the observed LCRS and for the four slices of the mock LCRS in redshift space (panel a, solid and dashed lines, respectively), for the L3-400 mock 2dF and the four slices of the mock LCRS in redshift space (panel b, solid and long dashed lines), and for the basic 'galaxy' catalogues and L3-400 mock 2dF in real spaces (panel c, solid and long dashed lines). Fits (4.2) and (4.3) are shown by thin solid lines in panels a, c & d.

The representativity of the mock 2dF results is corroborated by their comparison with those for the 'galaxy' distribution in the full simulation cube.

We define the mass function of structure elements as

$$W_m(\mu_m) = N_{mem}\frac{N_{cls}(N_{mem})}{N_{gal}}, \quad \mu_m = \frac{N_{mem}}{\langle N_{mem}\rangle}, \quad (4.1)$$

where N_{mem} is the richness, i.e., membership, in a cluster and $N_{cls}(N_{mem})$ the number of clusters possessing this richness, with normalising factor, N_{gal}, the total number of 'galaxies' in the sample. The corresponding cumulative mass functions,

$$W_m(\geq \mu_m) = \int_{\mu_m}^{\infty} d\mu_m \; W_m(\mu_m)\,,$$

are plotted in Fig. 4 for the six slices of the observed LCRS, for four slices of the L3-400 mock LCRS, for the L3-400 mock 2dF in real and redshift spaces and for the basic cubic volume-limited sample of simulation 'galaxies' in real space. The mass functions were, of course, corrected for radial selection effects.

In all cases, we find that rich clusters with $\mu_m \geq 1$ contain ∼50% of galaxies. The mass functions of the LCRS and of the mock slices are approximately the same, with mean richness of $\langle N_{mem}\rangle = 12.8$ & 16.1, respectively. Fig. 4a shows that they can be roughly fitted to an exponents,

$$W_m(\geq \mu_m) \propto \exp(-0.5\mu)\,. \quad (4.2)$$

However, in comparison with the corresponding full mock 2dF catalog, Fig. 4b shows how the small thickness of the slices has strongly distorted the mass distribution. It indicates that the use of a slice geometry for a survey leads to the artificial breakup of richer walls into a system of smaller separate walls and clusters.

The mass functions for the mock 2dF L3-400 and L3-600 catalogs are also similar to each other. Even so, as we have just seen, they are very different from the mass function of the slices, being roughly fitted by the exponents

$$W_m(\geq \mu_m) \propto \exp(-\alpha\mu^{1/3}), \quad \langle N_{mem}\rangle \approx 100\,, \quad (4.3)$$

with $\alpha = 0.6 - 1.2$ for different samples. This behavior of the mass functions is consistent with the theoretical expectations.

The mass functions for the mock L3-400 and L3-600 catalogs are also similar to the mass function for the sample of 'galaxies' in the cubic volume-limited sample (Fig. 4c). But the mean richness of structure elements in this last catalog is only $\langle N_{mem}\rangle \approx 60$.

***

5 WALLS AND FILAMENTS IN DM AND MOCK CATALOGS

In the previous section, we studied the structure of full samples. In this and the next major section, we split the full sample into high density regions and low density regions to make a more detailed investigation. Again, we take the threshold linking length $b_{thr} = 1$ as the natural means of obtaining the structure elements. The problem now comes in identifying which elements belong to high density regions, with the remaining elements to be assigned to low density regions. Our choice of a richness threshold N_{th} which yields high density regions containing ∼ 45% galaxies stems from our earlier papers (DMRT, LCRS2, DDMT), but it was also an empirical choice. Our interest lies in the potential of our analyses for the description of large scale structure, and we shall find that, with our analyses, the high density regions can mainly be characterised as wall-like and the low density regions as mainly filamentary in nature. Thus, a much different division would seriously contaminate one or the other subsamples.

5.1 Identification of walls

To test the robustness of the identification of the richer clusters, which we expect to be mainly wall-like, high density regions were compiled for both real and redshift space. For L3-400, ∼80–85% of the galaxies in high density regions were common to both a real space and the corresponding redshift space clusters, whereas L3-600 contained only ∼65–75% such common galaxies. A similar test performed in DDMT for the DM distribution and for the mock catalogs (without selection effects) demonstrates that ∼75 – 80% of objects assigned to walls are common to both real and redshift spaces.

First of all, these results characterise the high level of objectivity in selecting high density regions and demonstrate that distortions caused by peculiar velocities does not affect more than ∼20% of the objects assigned to the high density regions. This would also indicate that at distances

$\gtrsim 400\,h^{-1}$ Mpc for the L3 mock 2dF catalog, there is a significant increase in the number of artificial clusters produced by the cluster finding algorithm. Furthermore, it can be seen from the number-redshift plots for the observed LCRS (Figs. 1a and b) that most galaxies, ∼80–90%, are to be found between 200 and $300\,h^{-1}$ Mpc, so that the most well defined walls will also be situated in this region. Clearly, then, the most robust results for the properties of walls are to be obtained using the smaller L3-400 sample, although we shall lose ∼40% of the galaxies from the L3-600 sample in doing so (Sec. 3.2).

5.2 Walls and filaments in the full cubic volume simulation

Here, we compare the MST properties of the high and low density regions from the DM distribution with those from the 'galaxy' distribution in the full simulation cube for the L3 model. In both catalogs, the high density regions were extracted using a threshold dimensionless linking length of $b_{th} = 1$ and a threshold richness N_{th} such that the high density regions contained $\approx 44\%$ of the objects. The complementary subsample of poorer structure elements contains all the remaining objects left over after this process. Clearly, the separation of high density regions from low density regions increases the resolution of the MST PDFs, permitting a more detailed examination of these subsamples than a simple analysis of the full sample as a whole can give. Since our interest here is in the MST description of the actual structure within these subsamples, the analysis was performed in real space only.

As before, it is sensible to make use of the dimensionless argument of the MST PDFs, $l_{MST}/\langle l_{MST}\rangle$, where

$$\langle l_{MST}\rangle = 0.27 \quad \& \quad 0.5h^{-1}\mathrm{Mpc}, \tag{5.1}$$

for the DM and 'galaxy' high density regions, respectively. For the subsamples of DM and 'galaxy' low density regions the mean edge lengths are naturally larger, being, respectively,

$$\langle l_{MST}\rangle = 0.95 \quad \& \quad 1.2h^{-1}\mathrm{Mpc}. \tag{5.2}$$

Comparing these MST PDFs of the high and low density subsamples plotted in Fig. 5 with those plotted in Fig. 2 for the full samples shows important differences. We recall that the MSTs of Fig. 2 characterised both the richer and poorer samples of clusters as simply both filamentary in nature. But here we see that a more complex situation actually prevails, as 'zooming in' to examine separately the high density regions and the low density regions now also reveals the presence of sheet-like structures or walls: the MST PDF for the densest parts of the high density regions – i.e., of the samples of richer clusters – is best fitted by Rayleigh functions, characteristic of walls. The distributions of the less dense parts of the high density regions remain similar to an exponential, characteristic of filaments (Figs. 5a &c).

The densest rich clusters fitted by the Rayleigh function contain ∼70% of the high density region DM particles and ∼50% of the high density region 'galaxies'; this is only ∼20 – 30% of objects from total DM and 'galaxy' populations. This means that these dense rich clusters are concentrated within the first 3–5 bins of Figs. 2a & b. Furthermore, in each of these full-sample MST PDFs there is a superposition of edge

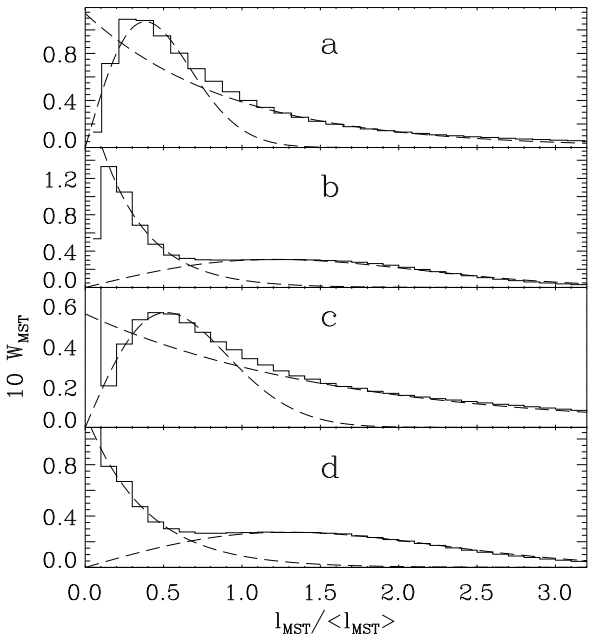

Figure 5. Distribution functions of MST edge lengths in real space for the sample of high density regions (panels a and c) and low density regions (panels b and d), separately, selected from the cubic volume-limited DM (panels a and b) and 'galaxy' (panels c and d) catalogs. Exponential and Rayleigh fits are plotted by dashed lines.

lengths from the high density regions with those from the low density regions, leading to a smearing of the individual high and low density region MST PDFs. Thus, in hindsight, it is not very surprising that the level of detail that we see in Fig. 5 may be lost when we combine the subsamples together to give the MST PDFs in Fig. 2.

These results agree well with theoretical expectations. The MST description for high density regions is consistent with a scenario in which walls at the present epoch have formed through large-scale compression, with successive merging of the richer filaments, of which some will be disrupted through violent relaxation (DD99, DDMT; also Paper 4, in preparation). Thus, walls are expected to be a complex random web of filaments and clusters, with some fraction of randomly distributed objects generated due to the disruption of filaments in the course of matter relaxation. The degree of relaxation of the matter compressed within walls and the fraction of objects attributed to clouds, filaments, and sheets depend upon the evolutionary path and will vary from wall to wall.

Similarly, we also see greater detail in the low density regions for the subsample of poorer clusters, but here we see the opposite effect from that seen above for the high density regions. The denser parts of the MST PDFs are still found to be exponential-like, while the less dense parts are well fitted to Rayleigh functions, as can be seen from Figs. 5b & d for the DM and 'galaxy' low density regions, respectively. In the low density regions, ∼70% of the DM particles and ∼45% of the 'galaxies' are concentrated in the densest filamentary-like clusters, i.e., low density region structure elements. Other objects assigned to low density regions could be naturally related to a low density sheet-like component and sheet-like haloes of denser filaments.

For low density regions, although the exponential distribution of the smaller edge lengths corresponding to filamentary structure seems natural, the appearance of a pancake-like part of the PDF at larger edge lengths may then be surprising. However, the smallest overdensities may still be in their earliest stages of formation of pancake-like haloes around nascent filaments. In this simulation they comprise ∼30–50% of the objects in low density regions. Of course, the process of the first pancake formation is most rapid at high redshifts and for the largest overdensities. But, in low density, i.e., low Ω_m, cosmological models, there remains with these smallest overdensities a trace of the process even now. Much later in the life of the universe, some of these pancakes will be transformed into filaments and some – due to expansion in the plane of the pancake rather than contraction – will disappear instead.

Comparing Figs. 5a & b with 5c & d shows how the biasing between 'galaxies' and DM has had only a slight quantitative effect on the MST PDFs. As was noted above, the densest rich clusters fitted in Fig. 5 to Rayleigh function contain ∼70% of the high density region DM particles and ∼55% of the high density region 'galaxies'. In the low density regions, ∼70% of the DM particles and ∼50% of the 'galaxies' are concentrated in the densest filaments. This difference between the DM and galaxy MST PDFs for small edge lengths – i.e., for the rich cores of clusters – of course reflects the 'anti-biasing' procedure used in identifying which DM particles are 'galaxies'. In particular, we note, as we did also in Sec. 4.1.1, the suppression of the cores of DM clusters to produce less steep high density cores for the 'galaxy' clusters. The difference also reflects the sensitivity of the MST analysis to variations among samples, with the 'galaxies' here a ∼1-in-4 random sampling of the DM particles according to probabilities laid down by the biasing algorithm. Our main concern in this paper, however, is in the morphological characterisation of large-scale structure that the MST analysis provides. Thus, the morphologies of 'galaxy' and DM structure elements are found to be very similar.

5.3 'Galaxy' distributions in mock catalogs

The results for the mock catalogs compared to those in Sec. 5.2 allow us to investigate the effect caused by a wedge-shaped geometry and the galaxy selection function. Thus, we plot in Fig. 6 the MST PDFs for the high and low density region subsamples in the mock 2dF L3-400 'galaxy' catalog corrected for the selection effect for both real and redshift space. The mean edge lengths for high density regions and low density regions in 'modified' catalogs are given by equations (6.1) and (6.2). (Recall, in this context, a 'modified' catalog is one whose coordinates have been transformed according to eq. (2.5) to account for the radial selection function.)

The first thing to note is that the distributions are little affected by whether we use the actual catalog or the 'modified' one (Sec. 4). However, the comparison of Figs. 6a & b with Figs. 5c & d do show a significant distortion due to the action of these factors. Thus, even the use of the 'modified' catalogs cannot substantially remove the effects of the selection function.

The distortion is such that, in real space, the PDF for

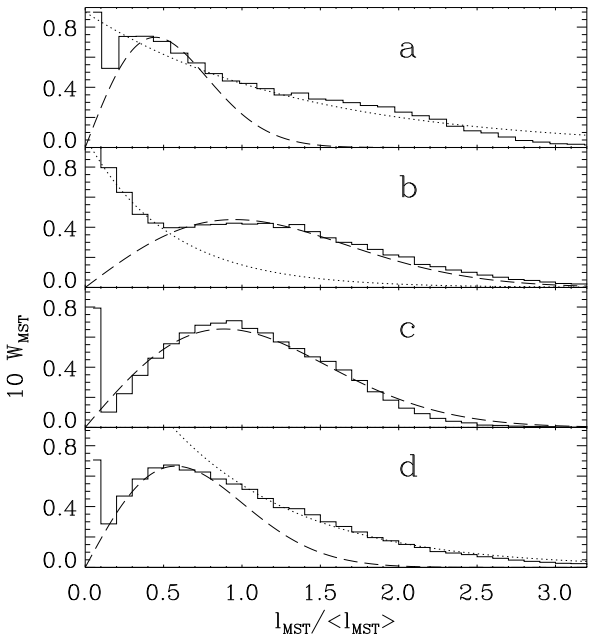

Figure 6. Distribution functions of MST edge lengths in real (panels a & b) and redshift (panels c & d) spaces are plotted for the samples of high density regions (walls, panel a & c) and low density regions (panels b & d), separately, for the L3-400 2dF mock catalog corrected for the selection effect. Rayleigh fits are plotted by long dashed lines, exponential fits are plotted by dotted lines.

the high density regions (∼44% of the 'galaxies' in sample L3-400) could almost be fitted by a single exponential. However, there is a hint that the high density part of the PDF (∼54% of the 'galaxies' in high density regions) is better fitted by a Rayleigh distribution, in which case we then obtain a composition of filamentary and sheet-like 'galaxy' populations similar to that found for the actual 'galaxy' distribution in the full simulation cube. The situation is clearer for the poorer clusters or low density regions. As for the actual 'galaxy' distribution, the high density part of the low density region, real space MST PDF (∼50% of low density region 'galaxies') is well fitted to an exponential function, while the lower density part of the PDF (also ∼50% of low density region 'galaxies') is similar to a Rayleigh distribution.

In redshift space, the PDF of the subsample of richer clusters is well fitted to a single Rayleigh function (Fig. 6c) in excellent agreement with results for the observational LCRS catalog (Sec. 6 of Paper 2) and with here, where Fig. 7'c shows that the main fraction of rich structure elements have $L_{tr}/L_{sum} \leq 0.3$. These results thus provide a quantitative insight into the appearance of walls in observational catalogs. The difference between the real and redshift space PDFs is of course due to the artificial merging and intermixture of neighbouring filaments due to the random peculiar velocities of the galaxies, and what we detect as a wall is mainly a complex fabric woven of filaments partly destroyed due to relaxation, along with a set of rich knots or clusters. We have here a quantitative description of the visual observation of walls projected on the sky like that of the Great Wall in Fig. 5a of Ramella, Geller & Huchra (1992). Furthermore, so strong is this effect – which is produced by only relatively

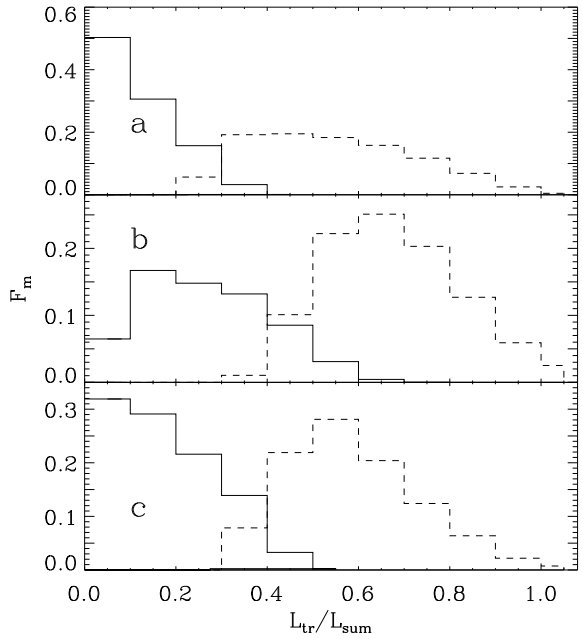

Figure 7. Mass distribution, F_m, of high density region (solid lines) and low density region (dashed lines) elements selected in real space for the cubic volume-limited DM (panel a) and 'galaxy' (panel b) catalogs and in redshift space for the L3-400 2dF mock catalog (panel c) versus the ratio of length of trunk and full length of tree, L_{tr}/L_{sum}.

small random velocities – that it also verifies the theoretical expectation of the strong compression and (partial) violent relaxation of matter within massive walls, leading to this crowding of the filaments within the walls.

For the subsample of poorer clusters or low density regions, both the high and low density parts of the redshift space PDF (∼60% and ∼40% of low density region 'galaxies', respectively) are well fitted to a Rayleigh distributions (Fig. 6d). For the high density part of low density region 'galaxies', the transformation of the real-space exponential distribution plotted in Fig. 6b to the Rayleigh distribution plotted in Fig. 6d can also be caused by artificial destruction and intermixture of filaments, again due to action of random velocities, of 'galaxies' composing high density filaments. This inference is consistent with results obtained in the next subsection (panel c in Fig. 7) where the main fraction of 'galaxies' assigned to low density regions is concentrated near the moderate values of $L_{tr}/L_{sum} \sim 0.5$–0.7 . For lower density part of low density region 'galaxies' the shapes of the MST PDFs plotted in Figs. 6 b & d are quite similar.

Thus, we conclude that even relatively small random velocities have a great effect on the internal characteristics of large-scale structure elements, enhancing the sheet-like nature of structure elements both in the high and low density regions. It is an effect that may need to be borne in mind when analysing observational catalogs.

5.4 Morphology of DM and 'galaxy' structure elements

As in Sec. 4.2.2, we can examine individual structure elements using a complementary method of characterising morphology, the ratio of length of trunk and full length of tree, L_{tr}/L_{sum}, to provide the mass distribution of structure elements as a function of this ratio. The distribution for the real space DM catalog is plotted in Fig. 7a, that for the real space 'galaxy' catalog in Fig. 7b and the mock L3-400 redshift catalog in Fig. 7c. In all cases, the mass distributions are similar to each other. In particular, the mass distribution obtained for the mock 2dF L3-400 catalog in redshift space is not very different to that obtained for the actual 'galaxy' distribution in the full simulation cube.

However, the remarkable result is how this characteristic so clearly differentiates between the morphologies of high density regions and low density regions. For high density regions the main fraction of structure elements have $L_{tr}/L_{sum} \leq 0.5$, while for low density regions values $L_{tr}/L_{sum} \geq 0.5$ are typical. The reasons for the peak of the distribution for low density region structure elements being at $L_{tr}/L_{sum} \approx 0.6$ rather than ≈ 1 are two-fold. Visually, we see that even the filaments in low density regions are part of a cosmic random network structure. $L_{tr}/L_{sum} \approx 1$ is only expected for separate filaments, while the presence of long branches and the connection of filaments to a cosmic network would decrease this ratio. Secondly, the results obtained with the MST PDF technique in the previous subsection shows the existence of high density clumps and lower density sheet-like haloes around filaments in low density regions and this also shifts F_m toward lower L_{tr}/L_{sum}.

6 WALLS AND FILAMENTS IN OBSERVATIONS AND SIMULATIONS

In this section, we wish to compare the properties of large scale structure in simulations with those of presently available observations. We expect that, because of its depth, the LCRS will provide a quite fair sample of walls – walls have a characteristic scale or mean separation of $\sim 50\,h^{-1}$ Mpc and the depth of the LCRS is $\sim 400\,h^{-1}$ Mpc. Even so, the slice geometry of the LCRS will have a significant effect on the results; hence, the need to apply all our methods of analysis to a mock slice catalog. *** ***

6.1 Division into high and low density regions

As in Sec. 5, we again use b_{thr}=1 and an N_{th}, so chosen so that f_{gal} ∼40–45% of the galaxies in the catalog will belong to the high density regions. The complementary low density region catalog consists, of course, of those galaxies that were not chosen as belonging to high density regions.

We applied this process to the 'modified' catalogs, which allows some account to be taken of the selection function (Sec. 2.4). The wall properties discussed here then become less sensitive to the depth of the catalog, allowing us to extend our catalogs to greater distances than if the analysis were to be applied directly to the unmodified catalog. However, as was discussed in Sec. 5.1, increasing depth also increases the number of spurious clusters. Thus, the full depth of the catalog cannot be used, as then the results will be contaminated by spurious clusters, and the modest increase that we have allowed for above provides fairly robust results. The catalogs analysed were then the observed LCRS, lim-

ited to a depth of $D = 450\,h^{-1}$ Mpc; the mock LCRS slices; and the L3-400 mock 2dF.

6.2 PDFs of MST edge lengths

Fig. 8 shows the MST PDFs of the high density regions, which are all well fitted by Rayleigh functions, characterising them as wall-like. As this is for the MST of the whole high density region sample, the PDFs provide more a description of the internal structure of walls than of their bounding surfaces. Thus, as the local overdensity is directly given by $l_{MST}/\langle l_{MST}\rangle$, i.e.,

$$n_{gal} \propto (l_{MST}/\langle l_{MST}\rangle)^{-3},$$

we see then that, with respect to the density distribution, all the walls are similar, with mean MST edge lengths,

$$\langle l_{MST}\rangle = 0.89,\ 0.81\ \&\ 0.87\text{Mpc}, \qquad (6.1)$$

for the observed LCRS, the mock LCRS, the L3-400 mock 2dF, respectively.

In more detail, it is interesting that the simulations seem to have a deficiency of shorter edge lengths, $l_{MST}/\langle l_{MST}\rangle \leq 1$, compared to the observations (Fig. 8b). Thus, with the present catalogs there are in the observations 6–7% more high density region galaxies in the high density clumps than are in the simulations. This is strange, since, due to the fibre separation limits inherent in the observed surveys (Shectman et al. 1996; Ratcliffe et al. 1996, 1998), one would expect relatively *fewer* galaxies in the high density regions of the observed catalogs, not in the simulations. On the other hand, the biasing scheme used in identifying 'galaxies' in the simulations suppresses the high density cores of the 'galaxy' clusters relative to the DM clusters; so perhaps this 'anti-aliasing' is too strong. Unfortunately, until more complete redshift surveys are done we shall not know if the present anti-biasing scheme in these simulations provides a good description of the cores of galaxy clusters. What is clear is how the MST PDF is proving to be a sensitive discriminator between the large-scale structure in simulated and observed catalogs.

Fig. 8c shows the significant difference caused by the different geometries of the mock LCRS and the mock 2dF, i.e., thin slices vs. a large area sky survey. *** *** The use of slices is expected to have a serious affect on the MST. Both the increase of $\langle l_{MST}\rangle$ (6.1) and the excess of larger edges seen in Fig. 8c in the high density regions of the L3-400mock 2dF sample relative to the high density regions of mock LCRS indicate some difference in estimated characteristics of these wall-like high density regions. It is quite a complex problem and the effect can only be determined empirically, as here. However, it serves as a reminder of the sensitivity of the MST to the spatial geometry of a survey.

The results plotted in Fig. 9 are for the low density regions in the observed LCRS, in the mock LCRS slices, and in the L3-400 mock 2dF sample. *** *** Again, the PDFs are all similar with respect to the density distribution, although now they characterise the low density regions as a mixture of filamentary and sheet-like structures. In all samples the PDFs for $l_{MST}/\langle l_{MST}\rangle \gtrsim 0.5$, involving 40–50% of low density region galaxies, are well fitted to exponentials, characteristic of a filamentary nature. However, the PDFs built for the L3-400 2dF mock sample and for the

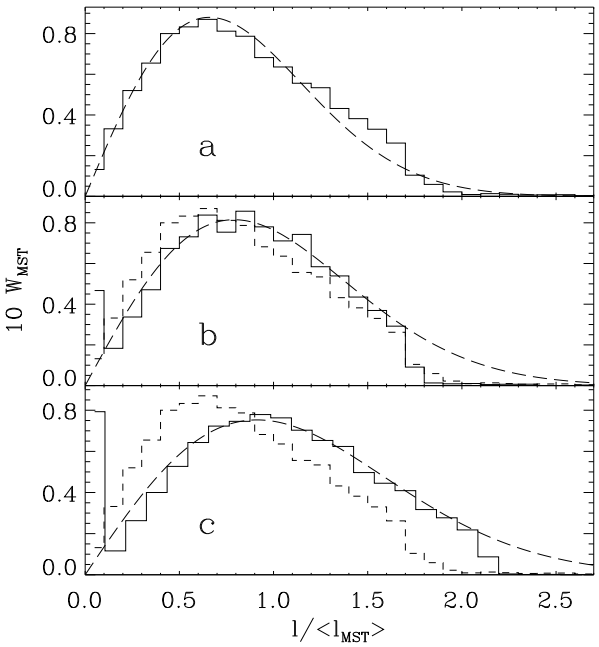

Figure 8. Distribution functions of MST edge lengths in redshift space corrected for radial selection effects are plotted for high density regions (walls) selected at b_{thr}=1 and $f_{gal} \approx 0.44$ in the observed LCRS(panel a, solid line, panels b & c, dashed lines), in the four mock LCRS slices (panel b, solid line), and in the L3-400 mock 2dF (panel c, solid line). The Rayleigh fits are plotted by long dashed lines.

observed and mock LCRS samples demonstrate noticeable differences. Thus, for the L3-400 mock 2dF the fraction of galaxies assigned to high density condensations and fitted to Rayleigh function contains ∼60% of galaxies in these low density regions instead of the ∼50% characteristic of the observed and mock LCRS samples. Moreover, for the L3-400 mock 2dF sample at larger edges lengths, the MST PDF can be equally well fitted by a Rayleigh function, which is consistent with results obtained in real space (Fig. 6d). For both the observed and mock LCRS samples, an exponential fit better characterizes the PDFs. This difference characterizes both the process of separation of high density regions and low density regions, the influence of thin slice geometry, and, perhaps, cosmic variance.

The mean MST edge lengths for these low density regions are

$$\langle l_{MST}\rangle = 1.84,\quad 1.61\ \&\ 1.49\ \ h^{-1}\text{Mpc}, \qquad (6.2)$$

for the LCRS, the mock LCRS, and the mock 2dF, respectively. Not surprisingly, these edge lengths are larger than those found for walls, Eq. (6.1). The sheet-like structures are, of course, seen for $l_{MST}/\langle l_{MST}\rangle \lesssim 0.5$, corresponding, thus, to the presence of high density clumps even in the low density regions and to the artificial intermixture of filaments with lower density haloes.

Importantly, however, we note the striking difference of the PDFs of Fig. 9 with those of Fig. 8. It serves to confirm the different morphologies of the high density regions from the low density regions and justifies the usefulness of our discrimination between these regions.

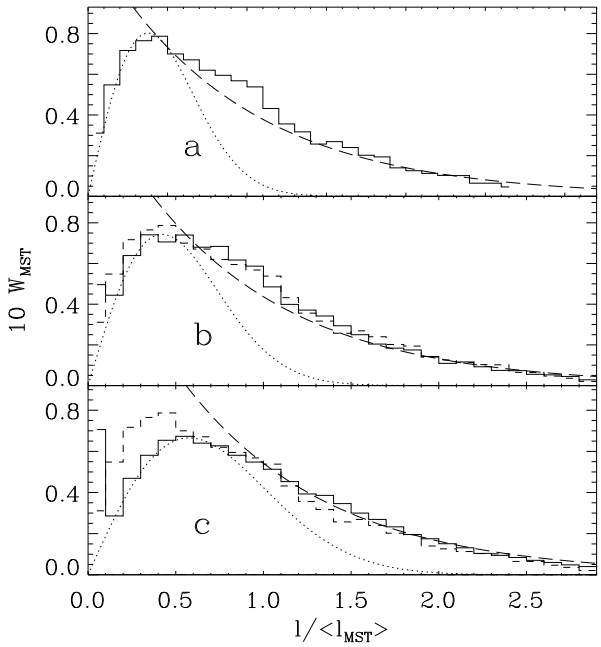

Figure 9. Distribution functions of MST edge lengths in redshift space corrected for the radial selection effects are plotted for low density regions selected at b_{thr}=1 in the observed LCRS (panel a, solid line, panels b & c, dashed lines), in the mock LCRS slices (panel b, solid line), and in the L3-400 mock 2dF (panel c, solid line). The exponential fits are plotted by long dashed lines, Rayleigh fits are plotted by dot lines.

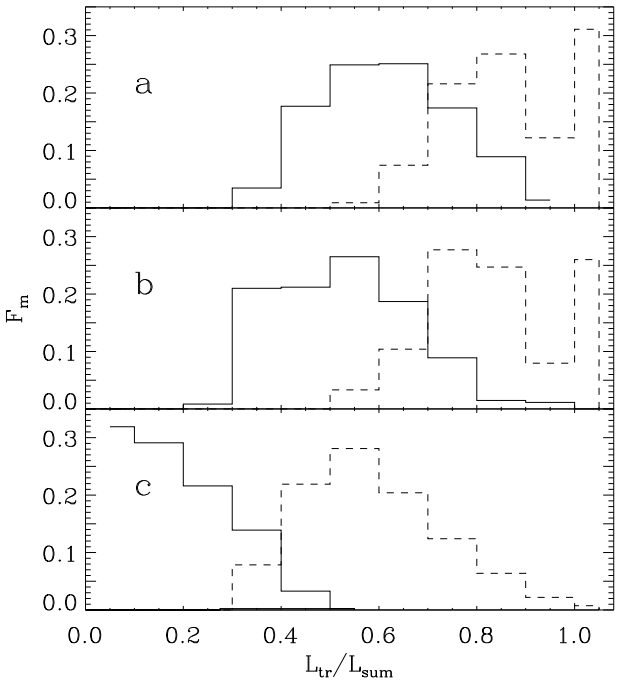

Figure 10. Mass distribution, F_m, of wall-like elements (solid lines) and filamentary component (dashed lines) selected in redshift space versus the ratio of length of trunk and full length of tree, L_{tr}/L_{sum}, for the observed LCRS (panel a), for the mock LCRS slices (panel b), and for the L3-400 mock 2dF (panel c).

6.3 Morphology of observed and simulated structure

Applying the MST to individual structure elements provides another, but completely different, means of characterising the morphology of large-scale structure. Thus, we investigate here the mass distribution of the separate elements in high density regions and in low density regions as a function of the ratio of the length of the MST trunk of a structure element to the full length of the tree, L_{tr}/L_{sum}. For the comparison with the observed LCRS catalog, the analysis is again performed in redshift space. The results are plotted in Fig. 10 for the observed LCRS, the mock LCRS, and the L3-400 mock 2dF 'modified' catalogs.

Rather nicely, Figs. 10a & b show that these mass distributions for the LCRS and the four simulated slices of the mock LCRS are, indeed, very similar to each other. In particular, they show the distinct difference in the morphological character this statistic gives for the high density regions and low density regions, and provides post-hoc support for our method of dividing a catalog into such regions. Thus, for high density regions the main fraction of objects is situated around $L_{tr}/L_{sum} \sim 0.5 - 0.6$, while for low density regions values $L_{tr}/L_{sum} \gtrsim 0.7$ are typical. These results are fairly consistent to those obtained with the MST PDF technique. In detail, however, the MST PDF shows a more significant difference between the results of the mock and observed LCRS.

In contrast, the mass distributions obtained for the mock 2dF sample are so completely shifted to smaller L_{tr}/L_{sum} that the low density region distribution for the full wedge catalog now occupies the space of the slices high density region distribution in this plot (Fig. 10c), with the wedge high density region structure elements becoming more explicitly sheet-like in character. Thus, this statistic is clearly much more sensitive to the different spatial geometries of the catalogs than is the MST PDF. In thin slices, both the large walls in high density regions and network of filaments in low density regions are very seriously artificially broken up by the slice geometry. Consequently, the wall-like structures in slices are less massive and the network of filaments a remnant, so that the decrease in L_{sum} is so much greater than for L_{tr}, resulting in the decrease of L_{tr}/L_{sum}.

7 SPATIAL DISTRIBUTION OF WALLS AND FILAMENTS

As we discussed in Sec. 2.5, a basic physical characteristic of a random spatial distribution is the mean free path between objects. Thus, we shall characterize walls by the mean free path, $\langle D_{sep} \rangle$, i.e., the average distance between the intersections of a random straight line with walls. It, evidently, also characterizes the size of voids, the space between walls. Indeed, it is perhaps the most appropriate way to do so, considering how random and broken large-scale structure is.

For the random network of filaments, the mean free paths along a random core sample depend linearly on the core size, from which the surface density of filaments, σ_f, is determined (Sec. 2.5.2).

In all cases, the 'modified' catalogs were used for the selection of structure elements to try to compensate as much as possible for the usual selection effects of a magnitude limited sample.

Table 2. Mean separation of the richer clusters.

D_{core}	N_{min}	N_{sep}	$\langle D_{sep}\rangle$ h^{-1}Mpc	σ_{sep} h^{-1}Mpc
Observed LCRS				
1.5°	1	773	42.2	39.3
1.5°	6	510	49.3	45.8
$10h^{-1}$Mpc	1	1063	40.6	47.2
$10h^{-1}$Mpc	6	944	47.1	51.7
Mock LCRS Slices				
1.5°	1	527	44.2	43.9
1.5°	6	375	51.6	44.2
$10h^{-1}$Mpc	1	453	46.8	78.2
$10h^{-1}$Mpc	6	446	47.9	80.4
L3-400 Mock 2dF				
1.5°	1	3090	35.9	29.1
1.5°	6	2502	37.5	35.5
$10h^{-1}$Mpc	1	1430	41.2	40.3
$10h^{-1}$Mpc	6	907	44.8	46.2

7.1 The Mean Free Path between walls

To estimate the mean free path between the walls in a catalog, radial conical cores of the space occupied by the catalog were constructed with an apex angle of $D_{core} = 1.5°$, i.e., a half-angle of 0.75°, corresponding to the beam size of the observed LCRS fields. Cylindrical cores, with a radial size $D_{core} = 10h^{-1}$ Mpc oriented across the line of sight, at fixed radial distance along arcs of right ascension, were also constructed. In each core, the galaxies of the high density regions were collected into point-like clusters placed at their centres-of-mass, as described in Sec. 2.5. The estimate of the mean free path is then just the average separation between these cluster points along the cores. To test the effect that the multiple intersections of the core with the random boundaries of an individual walls two minimal multiplicities of the clusters, $N_{min} = 1$ and $N_{min} = 6$, were used; for boundaries of a wall which twist and turn to multiply cut across a core, the limiting cluster multiplicity of $N_{min} = 1$ includes weaker intersections than will $N_{min} = 6$.

The mean separations of walls, $\langle D_{sep}\rangle$, and their dispersions, σ_{sep}, are listed in Table 2, where N_{sep} is the number of separations that were found. Results are stable enough, being weakly dependent on the linking lengths used for the cluster identification and upon the threshold richness of clusters. The results for radial cores and for cores oriented along arcs of right ascension are also quite similar. The larger value found for σ_{sep} for the mock LCRS of four slices of the simulation is caused by the small random fraction of extremely large separations. For the observed and mock LCRS the results obtained for the larger values of N_{min} are similar to those found in Paper 1 ($\langle D_{sep}\rangle \approx 53h^{-1}$Mpc). However, turning to the results for the simulated large sky area redshift survey, the L3-400 mock 2dF catalog, it seems that with the slice geometry a fraction of small separations, due to the multi-intersection of cores with the same wall, are missed, yielding a larger $\langle D_{sep}\rangle$ than for the large angle wedge catalog. The stability of the mock 2dF results bode well for the application of our analysis to forthcoming large redshift surveys, such as the real 2dF and the Sloan Digital Sky Survey.

As in all our previous analyses, we find that the distribution function of separations, $W(D_{sep})$, is well fitted to an exponential function, confirming the Poisson-like distribution of the separations of rich clusters along random core samples. For an exponential distribution, the dispersion is equal to mean, and, indeed, Table 2 does show them to be approximately equal for our distributions of separations.

Table 3. Mean separation and surface density of filaments.

N_{min}	N_{sep}	$\langle D_{sep}\rangle$ h^{-1}Mpc	σ_{sep} h^{-1}Mpc	$10^3 \cdot \sigma_f$ h^2Mpc^{-2}	D_{cell} h^{-1}Mpc
Observed LCRS, radial core, $\theta_{core} = 1.5°$					
1	3103	19.7	15.9	3.9	16.1
3	2092	26.4	24.4	2.9	18.5
5	1406	29.5	24.5	2.6	19.6
Observed LCRS, transversal core, $D_{core} = 10h^{-1}$Mpc					
1	2930	16.1	13.0	3.8	16.2
3	2626	17.7	15.6	3.4	17.1
5	2311	19.9	17.9	3.0	18.2
Mock LCRS Slices, radial core, $\theta_{core} = 1.5°$					
1	3064	19.5	16.8	3.9	16.1
3	2416	24.6	24.3	3.2	17.8
5	1687	32.5	31.1	2.4	20.6
Mock LCRS Slices, transversal core, $D_{core} = 10h^{-1}$Mpc					
1	2314	13.9	11.0	4.3	15.2
3	2271	14.0	11.1	4.3	15.2
5	2184	14.3	11.6	4.2	15.4
L3-400 Mock 2dF, radial core, $\theta_{core} = 1.5°$					
1	12225	14.1	13.2	5.4	13.6
3	8617	19.3	17.1	3.9	15.9
5	6697	27.1	24.2	2.8	18.7
L3-400 Mock 2dF, transversal core, $D_{core} = 10h^{-1}$Mpc					
1	7682	8.2	6.4	6.1	12.8
3	5692	12.0	9.9	4.2	15.4
5	5029	13.1	11.2	3.8	16.2

7.2 Spatial distribution of filaments

Core sampling analysis provides another complementary way of characterising the morphology of structure (see Sec. 2.5.2); we find that the results of the analysis follows well the relations of equations 2.7 a & b, thus characterising low density regions as simply filamentary. As these are poorer clusters than those in high density regions, they will be more sensitive to the observational constraints caused by the galaxy selection function discussed in Sec. 2.4 and by the spatial geometry that was surveyed.

With the measured mean free path, $\langle D_{sep}\rangle$, and core size, the surface density of filaments σ_f can then be estimated for the low density regions in the LCRS, mock LCRS and mock 2dF L3-400 catalogs. As in the previous section, a system of radial conical cores with the angular size 1.5° and a system of cylindrical cores across the line of sight with a radial size of $10\,h^{-1}$ Mpc were used.

The main results are listed in Table 3, where N_{sep}, $\langle D_{sep}\rangle$ and σ_{sep} are the number, mean value, and dispersion of the measured separations of the filaments in the core samples, from which the characteristic scale, $D_{cell} = \sigma_f^{-1/2}$, is then determined. Clearly, D_{cell} is an appropriate definition of the mean cell size of this random network of filaments. The formal precision of these estimates, ∼10%, is obtained from the comparison of the results for individual slices.

In more detail, we see that the estimates for σ_f for the radial conical cores and the transversal cylindrical cores are, indeed, approximately equal. All our estimates of σ_f lie between those obtained in Paper 1 for all filaments, $\sigma_f = (9.6 \pm 0.8) \cdot 10^{-3} h^2 \mathrm{Mpc}^{-2}$, and for the subpopulation of richer filaments, $\sigma_f = (1.4 \pm 0.3) \cdot 10^{-3} h^2 \mathrm{Mpc}^{-2}$. However, we remind the reader that in Paper 1 core sampling was applied to the full survey, whereas here we have separated the survey into low density regions and high density regions and applied the analysis to each separately.

Finally, it was found that, as for the walls of high density regions, the distribution of measured separations is also well fitted to an exponential one, confirming the Poisson-like character of the cluster distribution along a random core. And, of course, we can compare these results for the mock catalogs with those from their parent catalog, i.e., to

$$\sigma_f \approx 3.6 \cdot 10^{-3} h^2 \mathrm{Mpc}^{-2} \quad D_{cell} \approx 16.6 h^{-1} \mathrm{Mpc}$$

for the 'galaxy' filaments in the full simulation cube, as characterised by core sampling.

In summary, our results show that the mean cell size of the random filamentary network is $\sim$10–15 h^{-1} Mpc, with a Poisson-like distribution along a random core.

8 SUMMARY AND DISCUSSION

*** In this paper we have continued the investigation of the large scale matter distribution in simulated and observed catalogs which we began in Paper 1, Paper 2, DMRT, DD99, and DDMT. Application of the MST technique for the simulated basic DM and 'galaxy' distribution in the cubic volume and for the mock catalogs (Cole et al. 1998) allows to test numerical results and to reveal differences beteen these distributions. Comparison of these results with those obtained for the simulated and observed LCRS catalogs reveals the impact of slice geometry.

***

These surveys are deep enough and sampled well enough to provide for the first time a fairly representative sample of structure elements and, thus, reasonable measurements of structure properties. At the same time, however, the significant dependence of measured structure properties on the geometry and the richness of observed and simulated samples demonstrates that, with available surveys, we cannot yet obtain stable measurements of these properties. This inference becomes clear if one remembers that the mean separation between 'Great Walls' is $\sim$40– $50h^{-1}$Mpc and the number of walls in catalogs of depths $\sim(200 - 300h^{-1}\mathrm{Mpc})$ is very limited.

8.1 Large scale matter distribution in observations and simulations

Our analysis with the Minimal Spanning Tree technique demonstrates that, on large scales in both observed and simulated catalogs, galaxies and DM particles are strongly concentrated within a set of structure elements which can *roughly* be separated into sheet-like and filamentary subpopulations. The richer sheet-like (or wall-like) elements surround low density regions ('voids') with a typical size of about 40 – $50h^{-1}$Mpc. The 'voids' are occupied by a set of filaments and poorer, less massive pancakes which connect the richer walls to the joint (broken) network. In turn, the filaments are surrounded by low density sheet-like haloes. These conclusions are in general consistent with results obtained in our first analysis of the LCRS with the core-sampling method (Paper 1), with results obtained for the DM distribution (DMRT, DDMT), and with theoretical expectations (DD99).

The high concentration of DM and galaxies within randomly situated walls and filaments differs strongly from a 3-dimensional Poissonian distribution, and, in particular, this diffence generates the strong spatial correlations in galaxy distribution. Indeed, for the sample of galaxies randomly distributed along a suitable set of randomly distributed straight lines and planes, the two-point autocorrelation function is consistent with the observed power law, $\xi(r) \propto r^{-1.7}$ (van de Weygaert 1991; Buryak & Doroshkevich 1996). The correlation function becomes small at $r \geq 10h^{-1}$Mpc, but the strong modulation of the density of DM and galaxies is seen up to at least $r \sim 50h^{-1}$Mpc, which is the typical distance between the richer walls.

The large scale DM and galaxy distributions, however, are different in some important respects. First of all, galaxies contain only a few per cent of the matter in the Universe and their formation is sensitive to various biases. Moreover, in observations the large scale galaxy distribution and its measured properties are distorted by the influence of the survey geometry, selection effects, the random velocities of galaxies, and other random factors. The action of these factors cannot be estimated *a priori*, but the technique used here allows us to examine and to characterize these effects statistically.

The impact of some of these factors was reproduced in mock catalogs (Cole et al. 1998). Thus, comparison of characteristics of basic DM and volume-limited galaxy distributions in rectangular computational boxes reveals the influence of the simulation's galaxy identification algorithm. The comparison of these cubic volumes with mock 2dF and mock LCRS catalogs reveals the influence of the survey geometry and selection effects. The comparison of results obtained in real space and in redshift space revels influence of random velocities.

8.1.1 Correction for the selection effect

Unlike to action of other factors the influence of the galaxy selection function can be partly taken into account in our analysis. We do this by re-scaling the radial distance of the galaxies in order to obtain a pseudo volume-limited sample (Sec. 2.5). The resulting 'modified' catalogs are especially important in the estimates for the morphology and mass functions of the structure elements.

This correction, however, does not restore lost galaxies. and it only moderately increases – by about 20 – 30% – the richness of the sample under investigation. At large distances, even after such correction, some artificial structure elements are generated, thereby increasing the scatter and decreasing the robustness of the results.

This means that a poorer but more homogeneous sample of objects provides more reliable results and that attempts to compensate for the selection effects beyond certain limits is of only limited success.

8.1.2 Main properties of large scale matter distribution

Our analysis verifies that

(i) In real space in both basic DM and 'galaxy' cubic volume-limited catalogs, the matter distribution can be approximated by a superposition of two filamentary subpopulations with different typical number densities or typical edge lengths (Sec. 4.1.1). For the DM catalog, the high density subpopulation contains ∼90% of particles with the mean edge lengths ∼10 times smaller than that for the ∼10% of particles in the low density subpopulation. For the 'galaxy' catalog, the high density subpopulation contains ∼75% of objects with the mean edge lengths ∼3 times smaller than that for the ∼25% of particles in the low density subpopulation. These differences are indicative of the process of galaxy identification used in the simulations.

(ii) In mock catalogs in real space, the large scale 'galaxy' distribution can be approximated by a single filamentary population with a weak excess of objects at $l_{MST} \approx 1 - 1.5\langle l_{MST}\rangle$. However, for the mock catalog, the mean edge length is of about twice as compared with that for the 'galaxy' distribution from a cubic volume-limited sample (Table I). This difference in the large scale object characteristics is caused by galaxy selection effects and the spatial wedge geometry for a magnitude-limited sample. This difference cannot be eliminated using the 'modified' radial coordinates of Sec. 2.4, and it indicates that even for so rich a catalog as the 2dF some observed characteristics of the large scale matter distribution can be far from reality.

(iii) In both observed and mock catalogs in redshift space (Sec. 4.1.2), the large scale galaxy distribution can be approximated by a superposition of high density wall-like subpopulations (70 – 90% of objects) and lower density filamentary subpopulations. Properties of both subpopulations are weakly sensitive to the correction for the selection effects but depend heavily upon the sample geometry. Thus, the fraction of galaxies for MST PDFs fitted to Rayleigh functions (the sheet-like component) increases from ∼70% for the observed LCRS up to ∼80% for the mock LCRS and reaches ∼90% for mock 2dF catalogs.

(iv) The difference in the large scale object distributions in real and redshift spaces is caused by relatively small shifts in galaxy positions – $\sim \langle l_{MST}\rangle$ – due to their random radial velocities. This effect demonstrates the strongly nonhomogeneous spatial distribution of high density filaments selected in real space for basic catalogs. This result points out that the richer sheet-like structure elements were recently formed due to the collapse and further partial relaxation of previously formed high density filaments and clouds.

(v) The impact of a small slice thickness also strongly perturbs the observed properties of individual structure elements. In particular, the random crossing of structure elements with thin slices changes the measured morphology and mass function of these elements (Sec. 4.2.2).

8.2 Walls and filaments in observations and simulations

The division of the full samples into high density regions and low density regions, and the consequent analysis of these high density regions and low density regions separately permits a more detailed investigation of the large scale matter distribution. In particular, it allows the discrimination between the contribution of wall-like and filamentary condensations in high density regions and in low density regions for both real space and redshift space.

8.2.1 Identification of walls-like high density regions and filamentary low density regions

In all catalogs the high density richer structure elements (walls–like high density regions) were identified with richer clusters containing ∼40 – 45% of all objects at a given threshold linking length (or a given overdensity) as described in Sec. 2.2 . The subsamples obtained by the removal of high density region elements from the full sample were considered as subsamples of low density structure elements (low density regions).

Such a classification contains some degree of arbitrariness due to the continuous distribution of densities, morphologies, and other characteristics of the structure elements (see discussion in Sec. 2.3). Despite this limitation, this classification is still effective, and the comparison of the measured properties of high density regions and low density regions confirms that these are indeed two different populations. The objectiveness of this classification is also confirmed by the comparison of objects assigned to high density regions in real and redshift spaces. This test shows that, for all mock catalogs, ∼70 – 80% of galaxies assigned to high density regions in redshift space also appear in the corresponding high density regions in real space.

8.2.2 Walls and filaments in DM and unselected 'galaxies' catalogs

Results obtained in Sec. 5 show that, in real space, for all catalogs under consideration, subsamples of high density regions contain an essential sheet–like fraction (∼50% of galaxies and ∼70% of DM particles assigned to high density regions). For subsamples of low density regions the high density part (also ∼50% of galaxies and ∼70% of DM particles assigned to low density regions) is related to the filamentary component of the structure. These results confirm that the richer wall-like high density regions are formed due to compression of previously formed high density filaments. The partial relaxation of compressed matter leads to the partial disruption of the infalled filaments and stimulates formation of fraction of objects with a sheet-like MST PDF.

In contrast, in redshift space, the sheet-like population dominates in both high density regions and low density regions. Taking into account that, for the most part, the same objects appear in the high density regions independent of whether or not the classification was performed in real space or in redshift space (Sec. 7.2.1), we can relate the change of character of the object distribution to the artificial disruption and intermixture of neighbouring filaments caused by random radial velocities.

8.2.3 Walls and filaments in observed and mock catalogs

Results obtained for the observed LCRS and for the mock catalogs are in general quite consistent with each other and qualitatively coincide with those obtained for basic cubic

volume catalogs. Thus, in real space, about half of galaxies in high density regions are in the high density walls while the less dense component is filamentary. In contrast, in real space, the high density half of galaxies in low density regions are in filaments and the less dense part is rather sheet-like. As usual, in redshift space, sheet-like components dominate both in high density regions and low density regions.

For the LCRS and mock LCRS catalogs the thin slice geometry artificially reinforces the contribution of the filamentary component and distorts the measured mass function and structure morphologies (Secs. 6.2 and 6.3).

8.2.4 Morphology of observed and simulated structure

The comparison of morphology of structure elements selected in both high density regions and low density regions (Sec. 6.3 Fig. 10) for the observed LCRS, for the mock LCRS, and for the L3-400 mock 2dF, shows that the statistical characteristics of morphology are strongly dependent upon the geometry of the catalogs used. It shows that the artificial destruction of larger walls due to their intersection with the thin slices changes significantly the mass function and morphology of richer wall-like elements. For the random network of filaments, the same artificial destruction increases the number of separate filaments and a fraction of single galaxies.

8.2.5 Spatial distribution of wall-like and filamentary components

The free path between walls discussed in Sec. 6.4 provides an objective measurement of the size of low density regions in the galaxy distribution. This size, $\langle D_{sep}\rangle \approx 40 - 50h^{-1}$Mpc, is the same for the observed LCRS and for the mock catalogs and is consistent with what was found in Paper 1 using the core-sampling method. The approximate character of such estimates is caused by the procedure of wall identification and by the impact of several random factors such as the random multi-intersection of the core with a single wall.

The analysis of the spatial distribution of the filamentary component confirms that the typical cell size of the random network, $D_{cell} \approx 10 - 15h^{-1}$Mpc, is the same in both the radial and the transversal directions. So, the measured value of D_{cell} can be taken as a real characteristic of the random network formed by filaments.

8.3 General discussion

The theoretical analysis of structure formation and evolution in CDM-like models (DD99) has shown that it can be roughly described as a continuous formation of Zel'dovich' pancakes with progressively growing sizes and richness, and their simultaneous compression into high density filaments. The earlier formed structure elements, both pancakes and filaments, are involved in the process of hierarchical clustering and are brought into the richer pancakes. Further on, some of them are disrupted in course of relaxation, but survivors are seen as high density filaments and clumps embedded within richer walls and filaments.

This implies that the observed structure is always formed by the random superposition of structure elements with a various degree of filamentarity and 'wall-ness' and with progressively growing sizes and richness. Larger density contrast is typical for filaments formed due to the two dimensional compression of matter. The high degree of self similarity of this process can be expected up to later evolutionary stages when the disruption of structure into a system of high density clouds becomes dominant.

The continuous character of structure formation and the transformation of walls into filaments also implies the continuous distribution of structure element properties. The random shape of richer structure elements which are composed by both wall-like and filamentary components makes the classification of such elements somewhat arbitrary. In this sense, we prefer to characterize both an individual structure element and a set of such elements by the *degree of 'wall-ness'* or *the degree of filamentarity*. As was discussed above, this problem can be solved with the Minimal Spanning Tree technique applied for a full sample, for a selected structure element, or for a set of such elements.

This does not mean, however, that other descriptors cannot be used. Thus, although the Inertial Tensor method cannot successfully characterize the morphology of real structure elements, it does give us at least an objective measure of the size of such an element along its largest dimension. Further, the application of the core-sampling approach to a subsample of structure elements considered in DDMT allowed us to obtain a set of more accurate quantitative characteristics of wall-like elements and, moreover, to find some characteristics of the initial perturbations.

Promising results can also be obtained with Minkowski Functionals. This approach demonstrates high efficiency when it applied to CMB temperature maps (see, e.g., Schmalzing & Gorski 1998, Naselsky & Novikov 1998). The first applications of this approach to observed and simulated catalogs have shown that it can also give additional relevant information about large scale distributions in the Universe.

Acknowledgments

This paper was supported in part by Denmark's Grundforskningsfond through its support for an establishment of Theoretical Astrophysics Center. AGD also wishes to acknowledge support from the Center for Cosmo-Particle Physics "Cosmion" in the framework of the project "Cosmoparticle Physics".
This work was supported in part by the US Department of Energy under contract No. DE-AC02-76CH03000.

REFERENCES

Babul A., Starkman G.D., 1992, ApJ, 401, 28
Barrow J., Bhavsar S., Sonoda D., 1985, MNRAS, 216, 17
Baugh C.M. 1996, MNRAS, 280, 267
Baugh C.M., & Efstathiou G., 1993, MNRAS., 265, 145
Bharadwaj S. et al., 2000, ApJ, 528, 21
Bhavsar S., Ling E.N., 1988, 331, L63
Borgani S., 1996, Dark Matter in the universe, Varenna 1995, eds. S. Bonometto, J. Primack, A. Provenzale, p. 126
Buryak O., Demiański M., Doroshkevich A., 1991, ApJ, 383, 41
Buryak O., Doroshkevich A., 1996, A&A, 306, 1
Buryak O., Doroshkevich A., Fong R., 1994, ApJ., 434, 24

Cole S., Weinberg D.H., Frenk C.S., & Ratra B., 1997, MNRAS, 289, 37
Cole S., Hatton, S., Weinberg D.H. & Frenk C.S., 1998, MNRAS, 300, 945
Colless M.M., 1998, Phil. Trans. R. Soc. London A, in press
Collins, C.A., Heydon-Dumbleton, N.H., MacGillivray, H.T., 1989, MNRAS, 236, 7P
Collins, C.A., Nichol, R.C., Lumsden, S.L., 1992, MNRAS, 254, 295
Davis M., Peebles P.J.E. 1983, ApJ, 267, 465
de Lapparent V., Geller M.J., Huchra J.P., 1988, ApJ., 332, 44
Demiański M. & Doroshkevich A., 1999, ApJ., 512, 527
Demiański M. & Doroshkevich A., 1999, MNRAS., 306, 779, (DD99)
Demiański M., Doroshkevich A., Müller V., & Turchaninov V.I., 1999, MNRAS., in press, (DDMT)
Doroshkevich A., Tucker D.L., Oemler A., et al., 1996a, MNRAS, 284, 1281 (Paper 1).
Doroshkevich A.G., Müller V., Retzlaff J., & Turchaninov V.I., 1999, MNRAS, 306, 575, (DMRT).
Doroshkevich A. et al., 2000, MNRAS, 315, 767
Doroshkevich A.G., Tucker D.L., Fong R., Turchaninov V., & Lin H., 2001, MNRAS, 322, 369 (Paper 2)
Gott J.R., Melott A.L., Dickinson M., 1986, ApJ, 306, 341
Jenkins A. et al., 1998, ApJ., 499, 20
Kendall M., & Moran P., 1963, Geometrical Probability, (London: Griffin)
Kruskal J.B., 1956, Proc. Amer. math. Soc., 7, 48
Landy S.D. et al., 1996, ApJ, 456, L1
Monaco P, Efstathiou G., 1999, MNRAS, 308, 763
Naselsky P.D., Novikov D.I., 1998, ApJ, 501, 31
Oort J.H., 1983a, Ann.Rev.Astron.Astrophys., 21, 373
Oort J.H., 1983b, A&A, 139, 211.
Peebles, P.J.E., 1993, Principles of Physical Cosmology, Princeton Univ. Press, Princeton, New Jersey
Prim R.C., 1957, Bell. System Tech. J., 36, 1389
Ramella M., Geller M.J., Huchra J.P., 1989, ApJ, 344, 57
Ramella M., Geller M.J., Huchra J.P., 1992, ApJ, 384, 396
Ratcliffe, A. et al., 1996, MNRAS, 281, L47
Ratcliffe, A., Shanks, T., Parker, Q.A. and Fong, R., 1998, MNRAS, 296, 173
Sahni V., Sathyaprakash B.S., Shandarin S.F., 1997, ApJ, 476, L1
Sahni V., Sathyaprakash B.S., Shandarin S.F., 1998, ApJ, 495, L5
Sathyaprakash B.S., Sahni V., Shandarin S.F., 1996, ApJ, 462, L5
Sathyaprakash B.S., Sahni V., Shandarin S.F., 1998, ApJ, 508, 551
Schmalzing J., Gorski K.M., 1998, MNRAS, 297, 355
Schmalzing J., Gottlöber S., Klypin A., Kravtsov A., 1999, MNRAS, 309, 568
Schmalzing J., Diaferio A., 2000, MNRAS, 312, 638
Shandarin S., Zel'dovich Ya.B., 1989, Rev.Mod.Phys., 61, 185
Shandarin S., Yess. C., 1998, ApJ, 505, 12
Shectman S.A. et al., 1996, ApJ, 470, 172
Splinter R.J., Melott A.L., Shandarin S.F., Suto Y., 1998, ApJ, 497, 38
Thompson L.A., Gregory S.A., 1978, ApJ, 220, 809
Tucker D.L. et al., 1997, MNRAS, 285, L5
van de Weygaert R., 1991, Ph.D. Thesis, University of Leiden
Vishniac E.T., 1986, in Kolb E.W., Turner M.S., Lindley D., Olive K., Seckel D., eds., Inner Space/ Outer Space. University Chicago Press, Chicago, p. 190
White S.D.M., 1979, MNRAS, 186, 145
Zel'dovich Ya.B., 1970, A&A, 5, 20
Zel'dovich Ya.B., Einasto J., Shandarin S., 1982, Nature, 300, 407